A hybridized continuum-discontinuum modeling for investigating the fracture and energy evolution characteristics of rock mass under sequential explosive detonation using a bilinear cohesive fracture model

Qindong Lin [a], Xinguang Zhu [b,*], Jianfei Yuan [a], Chun Feng [b], Yundan Gan [a], Wenjun Jiao [a], Yulei Zhang [a]

[a] Xi'an Modern Chemistry Research Institute, Xi'an, Shaanxi 710065, China
[b] Key Laboratory for Mechanics in Fluid Solid Coupling Systems, Institute of Mechanics, Chinese Academy of Sciences, Beijing 100190, China

ABSTRACT

Modelling the dynamic mechanical response of rock mass under sequential explosive detonation, especially the fracture and energy evolution characteristics, is the key to optimizing the spatial distribution and initiation time interval of explosives. A hybridized continuum-discontinuum element method and energy statistics algorithm are implemented in this study to accurately investigate the rock dynamic response induced by sequential detonation loading. Based on the rock fracture status and the stress–strain curve of bilinear cohesive fracture model, an energy statistics algorithm considering all energy components is first proposed, and its accuracy and robustness are verified. Then, the continuum-discontinuum element method and energy statistics algorithm are adopted to simulate the dynamic response of rock mass under sequential detonation loading. The results indicate that the area of cracked interfaces generated by each explosive first increases and then decreases, which caused by explosive 2 is the largest, accounting for 38.19%. Due to the damage to rock caused by the previous detonation loading, the rock around explosive 1 mainly undergoes shear fracture, while the rock around explosives 2 and 3 mainly undergoes tensile fracture. The change trends of various energy components are different, and the explosion energy is mainly converted into friction energy and element kinetic energy.

1. Introduction

In the fields of mining, slope and tunnel engineering, blasting techniques have become an efficient and effective measure to break rock masses in the past few decades, and they have gradually evolved from single-hole blasting to multiple-hole blasting. For multiple-hole blasting, the spatial distribution distance and initiation time interval of explosives are key control parameters. To enhance the fragmentation effect of the rock mass and reduce the detrimental effect on the surrounding facilities as much as possible, it is necessary to first model the dynamic mechanical response of the rock mass under detonation loading, which lays the foundation for optimizing the control parameters of multiple-hole blasting and improving the utilization efficiency of explosion energy (Chen et al., 2021; Zhou et al., 2021; Bhagat et al., 2022).

Since laboratory and field experiments have the disadvantages of being expensive and time-consuming, numerical simulation has become a promising alternative method to investigate the blast-induced dynamic response of rock. Based on the differences in their inherent assumptions, numerical algorithms are categorized into continuum-based algorithms (e.g., FEM, XFEM, CEM, PD, and DDM) (Qin et al., 2021; Abdollahipour et al., 2016; Rezanezhad et al., 2019; Abdollahipour and Marji, 2020; Han et al., 2020b; Zhang et al., 2020b), discontinuum-based algorithms (e.g., DEM and DDA) (Ni et al., 2020; Wang and Nguyen, 2022) and mesh-free algorithms (e.g., SPH and MPM) (Jayasinghe et al., 2019; Wang et al., 2021a). Since each numerical algorithm has some limitations, an increasing number of coupled algorithms (e.g., FEM/DEM, DEM/SPH, DDA/SPH, FEM/SPH) have been proposed (Wu et al., 2018; Ai and Chen, 2020; Liu et al., 2020; Mardalizad et al., 2020; Peng et al., 2021).

Based on the numerical algorithms mentioned above, scholars have simulated the dynamic response of rock mass under detonation loading and investigated the trends of the variations in different mechanical parameters. Hajibagherpour et al. (2020) numerically studied the mechanism of rock fragmentation due to blast-induced shock waves in a

single blasthole by a 2D discrete element code, and the numerical result was in good agreement with the experimental result. Zhu and Zhao (2021) presented a nonordinary peridynamics computational approach to model blast-induced rock fractures, and the fracturing process of rock was assessed based on both the JH2 damage model and tensile failure model. Gharehdash et al. (2020) investigated the blast-induced fracture process of Barre granite using a penalty-based contact treatment in smoothed particle hydrodynamics along with variable particle resolutions. Bird et al. (2023) presented a 3D nonlinear finite element model to study the fracture intensity caused by blasting, which is able to handle damage to rock due to both compression and tension. Ma et al. (2022) analysed the pressure of the hole wall, energy evolution and crack propagation during blasting and found that the strain energy of rock mass and the area of blast-induced cracks are negatively correlated with the uncoupling coefficient of the charge. Lak et al. (2019a, 2019b) simulated the dynamic fracture process in a jointed rock mass based on the dual fracture media approach and discrete element method, and the results indicated that the deployed procedure is able to model the different fracture propagation patterns observed in rock mass. Banadaki (2011) numerically studied the stress field and blast-induced dynamic fracture in Barre and Laurentian granites, and JH2 strength and failure models along with polynomial EOS were adopted. Alizadeh et al. (2023) investigated the dynamic response of heterogeneous geomaterials under cyclic loads based on the 2D boundary element method. Based on the dynamic finite element model, Jiang et al. (2023) proposed that tensile cracks dominate the damage of discontinuity tips in the initial stage after detonation, while shear cracks may dominate near the end of blasting. Some scholars have conducted research on the cumulative damage of rock under repeated blast loading. Wang et al. (2021b) found that repeated blast loading contributes little to rock breakage in the direction of the minimum principal stress and that the cracks mainly propagate along the direction of the maximum principal stress. Han et al. (2020a) studied the damage evolution of rock during contour blasting in the bench of a deeply buried tunnel and found that the in situ stresses impeded the blast-induced damage evolution.

In the numerical simulation of the dynamic response of rock under blast loading, how to accurately characterize the initiation and propagation of cracks is a research focus. Due to the advantages of complete theoretical derivation, convenience of implementation and avoiding stress singularity, the cohesive zone model is widely adopted to simulate the dynamic fracture process of rock (Cordero et al., 2019; Saadat and Taheri, 2019; Nairn and Aimene, 2021). Within the framework of the combined finite-discrete element method and ICEM-based cohesive elements, Fukuda et al. (2021) studied the dynamic fracture process of marbles in dynamic BTS tests and UCS tests. Han et al. (2023) used the combined finite-discrete element method to model the rock fracture process induced by single-hole destress blasting and found that the fractures shift the high abutment pressure from the tunnel face. Wang et al. (2021c) introduced the methodology of compiling the rate-dependent model for cohesive elements via a user subroutine, and the sensitivity of the dynamic branching model results to the element size, mesh structure and material parameters was discussed.

Currently, numerical research on the dynamic response of rock mass under detonation loading has two deficiencies. First, most of the adopted numerical methods are continuum-based and mesh-free methods. The continuum-based method simulates the dynamic expansion process of cracks mainly by deleting elements, which has the disadvantages of not following the laws of conservation of energy, mass and momentum. The mesh-free method has difficulty accurately characterizing the initiation and propagation process of cracks. Therefore, the adopted numerical methods have difficulty accurately simulating the dynamic mechanical response of rock mass under detonation loading. Second, the researchers only investigated the change characteristics of rock deformation energy and kinetic energy without studying other types of energy (e.g., fracture energy, friction energy), which limits the study of the utilization efficiency of explosion energy.

To accurately model the dynamic mechanical response (e.g., displacement, fracture) of rock mass under sequential detonation loading and obtain the complex conversion process of explosion energy, the continuum-discontinuum element method (CDEM) and energy statistics algorithm are implemented in the study. Compared with other numerical algorithms, CDEM achieves the conservation of energy, mass and momentum during the initiation and propagation of cracks, which is essential for accurately modelling the dynamic response of rock mass. In addition, the energy statistics algorithm achieves the accurate statistics of various energy components in the rock mass. First, the energy statistics algorithm for the bilinear cohesive fracture model is established. Then, the accuracy and robustness of the energy statistics algorithm are verified. Finally, a full-time numerical simulation of rock mass under sequential detonation loading is conducted, and the displacement, fracture and energy evolution characteristics are quantitatively analysed, which lays the foundation for optimizing the spatial distribution and initiation time interval of explosives.

2. Methodology

2.1. Continuum-discontinuum element method

As a dynamic explicit numerical method, the continuum-discontinuum element method (CDEM) is established based on the Lagrangian energy system. To improve the applicability of solving large-deformation problems, CDEM adopts the dynamic relaxation method for explicit iterative solutions. Since the initiation and expansion of cracks are not realized by deleting elements in CDEM, it follows the laws of conservation of energy, mass and momentum (Zhang et al., 2020a; Lin et al., 2022b). The basic numerical model in CDEM includes blocks and interfaces, as shown in Fig. 1. The interfaces include the real interfaces (denoted by the black solid lines in Fig. 1(a)) and the virtual interfaces (denoted by the red solid lines in Fig. 1(a)). The real interfaces are used to represent the real discontinuous features (e.g., joints, faults) of the material. The virtual interface (as shown in Fig. 1(b)) has two main functionalities: to connect blocks and transfer mechanical information and to provide the potential space for crack initiation and propagation. To improve the efficiency of contact detection and simplify the calculation of contact force, the semi-spring and semi-edge combined contact model (as shown in Fig. 1(c)) is introduced (Feng et al., 2014).

According to the Lagrangian theory of energy systems, the governing equation of CDEM is established as follows:

$$\frac{d}{dt}\left(\frac{\partial L}{\partial \dot{u}_i}\right) - \frac{\partial L}{\partial u_i} = Q_i \tag{1}$$

where Q_i denotes the nonconservative force of the Lagrangian system, u_i denotes the displacement, and $\dot{u}_i$ denotes the velocity. L denotes the energy functional of the Lagrangian system, which is written as

$$L = \prod_m + \prod_e + \prod_f \tag{2}$$

where Π_m, Π_e and Π_f denote the systematic kinetic energy, the systematic deformation energy and the work of conservative force, respectively.

Taking an element in the Lagrangian system as the research object, the energy functional of the element is written as

$$L = \int_V \frac{1}{2}\rho \dot{u}_i^2 dV + \int_V \frac{1}{4}\sigma_{ij}(u_{i,j} + u_{j,i})dV - \int_V f_i u_i dV \tag{3}$$

where ρ denotes the element density, σ_{ij} denotes the element stresses, $u_{i,j}$ denotes the derivative of displacement u_i in the j direction, $u_{j,i}$ denotes the derivative of displacement u_j in the i direction, f_i denotes the body force of the element node, and V denotes the element volume.

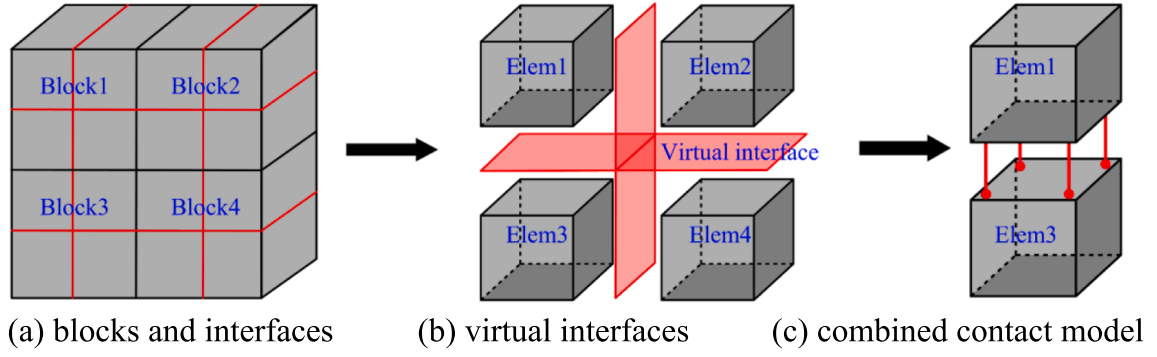The nonconservative force includes the damping force Q_μ and

(a) blocks and interfaces   (b) virtual interfaces   (c) combined contact model

Fig. 1. Basic numerical model in CDEM.

external force $Q_{\overline{T}}$, which is defined as

$$Q_\mu = \int_V \mu \dot{u}_i dV, \quad Q_{\overline{T}} = -\int_S \overline{T}_i dS \tag{4}$$

where μ denotes the damping coefficient and $\overline{T}_i$ denotes the surface force at the element boundary.

Substituting Eq. (2) to Eq. (4) into Eq. (1) yields

$$-\left(\int_V \rho \ddot{u}_i dV + \int_V \sigma_{ij} \frac{\partial u_{i,j}}{\partial u_i} dV - \int_V f_i dV\right) = \int_V \mu \dot{u}_i dV - \int_S \overline{T}_i dS \tag{5}$$

where $\ddot{u}_i$ denotes the acceleration.

Using the partial integration expression (as shown in Eq. (6), the Lagrangian equation Eq. (5) is simplified to Eq. (7).

$$\int_V \sigma_{ij} \frac{\partial u_{i,j}}{\partial u_i} dV = \int_S \sigma_{ij} n_j dS - \int_V \sigma_{ij,j} dV \tag{6}$$

$$\int_V \left(\sigma_{ij,j} + f_i - \rho \ddot{u}_i - \mu \dot{u}_i\right) dV + \int_S \left(\overline{T}_i - \sigma_{ij} n_j\right) dS = 0 \tag{7}$$

Eq. (7) can be solved numerically based on the FEM. The internal force acting on the element node is equal to the partial derivative of the element deformation energy with respect to the nodal displacement, which is written as

$$F_i^e = \frac{\partial \Pi_e}{\partial u_i} = K_{ij}^e u_j \tag{8}$$

where K_{ij}^e denotes the element stiffness matrix.

The Lagrangian equation is transformed to

$$\int_V \rho \ddot{u}_i dV + \int_V \mu \dot{u}_i dV + F_i^e = \int_V f_i dV + \int_S \overline{T}_i dS \tag{9}$$

Finally, the governing equation of the element is written as Eq. (10). Solving the governing equation Eq. (10) is the core of the CDEM computation, and it is solved based on the explicit Euler forward difference method.

$$\mathbf{M}a(t) + \mathbf{C}v(t) + \mathbf{K}u(t) = \mathbf{F}(t) \tag{10}$$

where $a(t)$, $v(t)$ and $u(t)$ denote the acceleration vector, velocity vector and displacement vector, respectively. $\mathbf{M}$, $\mathbf{C}$, and $\mathbf{K}$ denote the mass matrix, damping matrix and stiffness matrix, respectively. $\mathbf{F}(t)$ denotes the external force vector.

2.2. Contact detection algorithm

For the 3D block discrete element method, the direct method, common plane method, penetration edge approach and incision body scheme are the four typical algorithms for detecting the contact between blocks. To simplify the contact detection procedure and improve the

contact detection accuracy, a semi-spring and semi-edge combined contact detection algorithm is proposed and introduced into the CDEM (Feng et al., 2014).

For the 3D block contact, there are six contact types. vertex to vertex, vertex to edge, vertex to face, edge to edge, edge to face and face to face. In the semi-spring and semi-edge combined contact detection algorithm, to detect the target edge and target face easily, the vertices and edges of block indent to each face, as shown in Fig. 2, and the semi-spring and semi-edge are created subsequently. Based on this algorithm, the six contact types are simplified to two contact types, i.e., semi-spring and target face contact, semi-edge and target edge contact.

2.2.1. Semi-spring contact algorithm

For the semi-spring and target face contact, two contact cases can be found: (I) the distance d between the semi-spring and target face is less than the searching tolerance d_{st}, and the projection point of the semi-spring is located within the target face; (II) the semi-spring is located within the block.

For case I, the distance d between the semi-spring and target face is obtained by Eq. (11), which is written as

$$d = \left| \overrightarrow{n_f} \cdot \left(\overrightarrow{P_s} - \overrightarrow{C_f} \right) \right| \tag{11}$$

where $\overrightarrow{n_f}$ denotes the unit outwards normal vector of the target face, $\overrightarrow{P_s}$ denotes the coordinate of the semi-spring, and $\overrightarrow{C_f}$ denotes the coordinate of the target face centre.

Once the distance d is less than the searching tolerance d_{st}, Eq. (12) is adopted to judge whether the projection point of the semi-spring is located within the target face. If the projection point is located within the target face, J_{ijk} should be 1 for any composition of vertices i, j and k.

$$J_{ijk} = \left(\overrightarrow{V_{si}} \times \overrightarrow{V_{sj}} \right) \cdot \left(\overrightarrow{V_{sj}} \times \overrightarrow{V_{sk}} \right) \tag{12}$$

where i, j, and k are three vertices of the target face in the clockwise direction. $\overrightarrow{V_{si}}$ denotes the relative coordinate vector pointing from
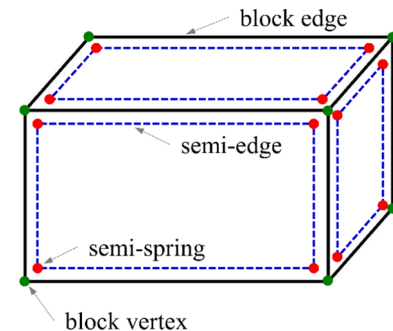

Fig. 2. Schematic diagram of the semi-spring and semi-edge.

vertex s to vertex i.

For case II, Eq. (13) is adopted to judge whether the semi-spring is located within the block. If $JC > 0$ is satisfied for any face of the block, the semi-spring is located within the block. Once it is determined that the semi-spring s is located within the block, the face of the block nearest to the semi-spring is regarded as the target face.

$$JC_i = \overrightarrow{V_{si}} \cdot \overrightarrow{n} \tag{13}$$

where $\overrightarrow{V_{si}}$ denotes the relation coordinate vector pointing from semi-spring s to the centre of face i.

2.2.2. Semi-edge contact algorithm

To search the target edge of the semi-edge, the target face where the target edge is located is found first. All the faces of the potential blocks are looped, and the most likely face of the potential blocks is determined by Eq. (14).

$$PF = \min\left(\overrightarrow{n_m} \cdot \overrightarrow{n_p}\right) \tag{14}$$

where PF denotes the most likely face where the target edge is located, $\overrightarrow{n_m}$ denotes the unit outwards normal vector of the face where the semi-edge is located, and $\overrightarrow{n_p}$ denotes the unit outwards normal vector of the probable face.

Once the most likely face PF is found, each edge of the face PF is judged whether it is parallel to the semi-edge or not based on Eq. (15). If $PF_p < 1$, these two edges are not parallel.

$$PF_p = \left|\overrightarrow{V_{mm}} \cdot \overrightarrow{V_{tt}}\right| \tag{15}$$

Eq. (16) is adopted to calculate the distance d_e between these two edges.

$$d_e = \left|\left(\overrightarrow{V_{mm}} \times \overrightarrow{V_{tt}}\right) \cdot \overrightarrow{V_{mt}}\right| \tag{16}$$

If $PF_p < 1$ and $d_e < d_{st}$, the edge is regarded as the target edge, and the intersection between the target edge and semi-edge is judged. The co-ordinates of semi-edge and target edge are projected to a plane with the normal vector $(\overrightarrow{V_{mm}} \times \overrightarrow{V_{tt}})$. On the projection plane, the intersection point is obtained first. Once the intersection point is located inside two edges at the same moment, the contact between the target edge and semi-edge will be established.

Based on the semi-spring contact and semi-edge contact, contact detection between 3D blocks is achieved, and the contact force is calculated. A more detailed algorithm introduction was written by Feng (Feng et al., 2014).

2.3. Bilinear cohesive fracture model

In the semi-spring and semi-edge combined contact detection algorithm, a local Cartesian coordinate system is created, and the contact force F of the numerical spring is decomposed into the tangential force F_{px} along the $\times$ direction, tangential force F_{py} along the y direction and normal force F_{pz} along the z direction. During the iterative computation of the contact force, F_{px}, F_{py} and F_{pz} are calculated independently. The trial normal force and trial tangential force at the next time step t_1 are first calculated, which is determined via

$$\begin{cases} F_{px}^{t_1} = F_{px}^{t_0} - k_s s_p \Delta u_x \\ F_{py}^{t_1} = F_{py}^{t_0} - k_s s_p \Delta u_y \\ F_{pz}^{t_1} = F_{pz}^{t_0} - k_n s_p \Delta u_n \end{cases} \tag{17}$$

where $F_{px}^{t_0}$, $F_{py}^{t_0}$ and $F_{pz}^{t_0}$ denote the tangential contact force, tangential contact force and normal contact force at the current time step t_0, respectively. $F_{px}^{t_1}$, $F_{py}^{t_1}$ and $F_{pz}^{t_1}$ denote the trial tangential contact force, trial tangential contact force and trial normal contact force at the next

time step t_1, respectively. k_n and k_s denote the normal contact stiffness and tangential contact stiffness per unit area, respectively. s_p denotes the sectional area of the numerical spring. Δu_n denotes the normal relative displacement increment from t_0 to t_1, and Δu_x and Δu_y denote the tangential relative displacement increment from t_0 to t_1.

The occurrence of tensile failure is determined based on Eq. (18). Once the tensile failure criterion is satisfied, the normal contact force and tensile strength are corrected.

$$\begin{cases} \text{if} \quad -F_{pz}^{t_1} \geq \sigma_{pt}^{t_0} s_p \\ \text{then} \quad F_{pz}^{t_1} = -\sigma_{pt}^{t_0} s_p, \sigma_{pt}^{t_1} = \dfrac{-\left(\sigma_{pt}^{t_0}\right)^2 u_n}{2G_{ft}} + \sigma_{pt}^0 \end{cases} \tag{18}$$

where σ_{pt}^0, $\sigma_{pt}^{t_0}$ and $\sigma_{pt}^{t_1}$ denote the tensile strength at the initial time step, current time step and next time step, respectively. G_{ft} denotes the tensile fracture energy.

The occurrence of shear failure is determined based on Eq. (19). Once the shear failure criterion is satisfied, the tangential contact force and cohesion are corrected.

$$\begin{cases} \text{if} \quad F_{ps}^{t_1} \geq F_{pz}^{t_1} \tan\varphi + c_p^{t_0} s_p \\ \text{then} \quad F_{ps}^{t_1} = F_{pz}^{t_1} \tan\varphi + c_p^{t_0} s_p, c_p^{t_1} = \dfrac{-\left(c_p^{t_0}\right)^2 u_s}{2G_{fs}} + c_p^0 \end{cases} \tag{19}$$

where c_p^0, $c_p^{t_0}$ and $c_p^{t_1}$ denote the cohesion at the initial time step, current time step and next time step, respectively. u_s denotes the tangential relative displacement at the current time t_0. φ denotes the friction angle. G_{fs} denotes the shear fracture energy. $F_s^{t_1}$ denotes the resultant tangential contact force at the next time step t_1.

According to Eq. (18) and Eq. (19), the normal and tangential stress–strain curves of the numerical spring can be drawn, as shown in Fig. 3.

3. Energy statistics algorithm

3.1. Energy classification

According to the failure state of the material and the basic characteristics of the CDEM model, Lin et al. (2022a) proposed the energy types in the model at different stages, as shown in Fig. 4. When the model is at the continuous stage, the energy includes the element deformation energy W_{EE}, element kinetic energy W_{EV}, spring deformation energy W_{PE}, damping energy W_D and gravitational potential energy W_G. With the appearance of cracks, when the model changes from the continuous stage to the discontinuous stage, spring fracture energy W_{PC} appears. When the model is at the discontinuous stage, the spring fracture energy W_{PC} disappears, and friction energy W_R appears.

To accurately investigate the evolution characteristics of various energy components, it is necessary to not only accurately judge the model stage to determine the energy types but also accurately calculate the values of various energy components. An energy statistics algorithm has been established and verified for the case of adopting the Mohr-Coulomb brittle fracture model as the interface constitutive model (Lin et al., 2022a). However, when the bilinear cohesive fracture model is adopted as the interface constitutive model, the statistical algorithm for spring deformation energy W_{PE}, spring fracture energy W_{PC} and friction energy W_R needs to be re-established. Moreover, the statistical algorithm for gravitational potential energy W_G was not established in the previous study. Therefore, this study needs to re-establish the statistics algorithm for W_{PE}, W_{PC}, W_R and W_G.
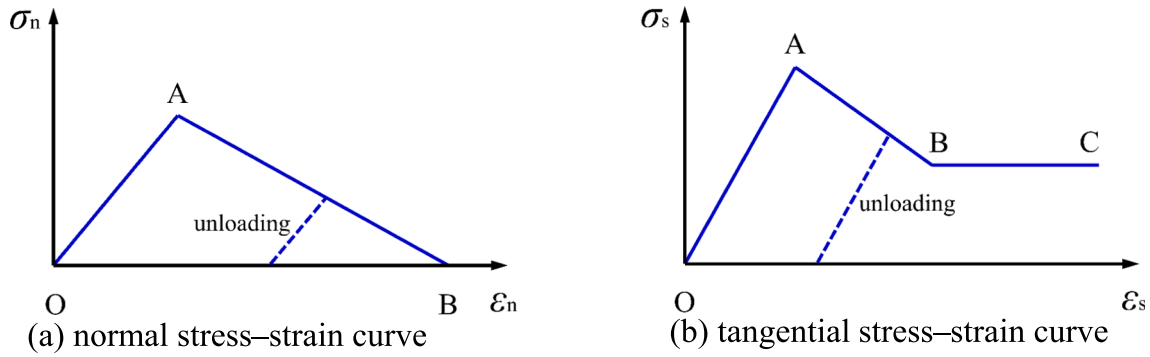
Fig. 3. Stress–strain curve of the bilinear cohesive fracture model.
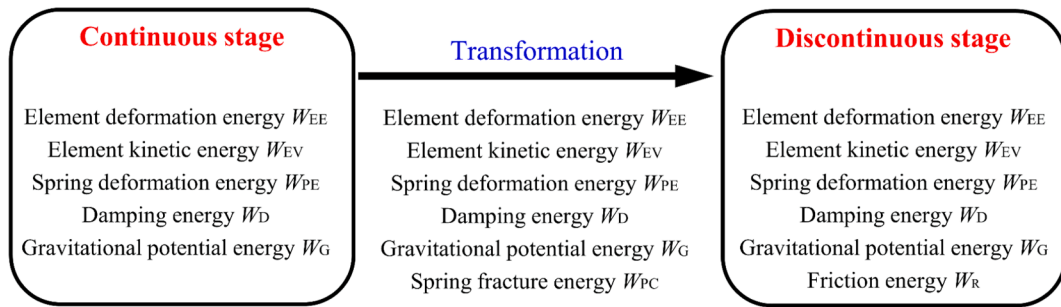

Fig. 4. Energy types at the different stages.

3.2. Detailed algorithm description

3.2.1. Spring deformation energy W_{PE}

In the bilinear cohesive fracture model, the spring deformation energy W_{PE} includes normal deformation energy w_{pet} and tangential deformation energy w_{pes}. The normal deformation energy w_{pet} is plotted in Fig. 5. For the elastic stage, the area of triangle ODE in Fig. 5(a) is equal to w_{pet}. For the softening stage, the area of triangle DFE in Fig. 5(b) is equal to w_{pet}. The tangential deformation energy w_{pes} is plotted in Fig. 6. For the elastic stage, the area of triangle ODE in Fig. 6(a) is equal to w_{pes}. For the softening stage, the area of triangle DFE in Fig. 6(b) is equal to w_{pes}. For the cracked stage, the area of triangle DFE in Fig. 5(c) is equal to w_{pes}.

To obtain the spring deformation energy W_{PE} of the entire model, first, the normal deformation energy w_{pet} is calculated based on Eq. (20). Subsequently, the tangential deformation energy w_{pes} is calculated based on Eq. (21). Finally, all springs are looped to obtain the spring deformation energy W_{PE} of the entire model (as shown in Eq. (22)).

$$w_{pet} = \frac{1}{2} \frac{\sigma_{pz}^2}{k_n} s_p \tag{20}$$

$$w_{pes} = \frac{1}{2} \left(\frac{\sigma_{px}^2}{k_s} + \frac{\sigma_{py}^2}{k_s} \right) s_p \tag{21}$$

$$W_{PE} = \sum_{k=1}^{N_p} \left(w_{pet} + w_{pes} \right) \tag{22}$$

where N_p denotes the number of numerical springs.

3.2.2. Spring fracture energy W_{PC}

3.2.2.1. Loading path. When the normal stress σ_{pz} reaches the tensile strength σ_{pt}, the normal stress–strain curve enters the softening stage, σ_{pt} decreases continuously, and it is determined that the spring undergoes tensile damage. Once σ_{pt} decreases to zero, it is determined that the spring undergoes tensile crack. For the resultant tangential stress σ_{ps}, when it reaches the shear strength σ_s, the tangential stress–strain curve
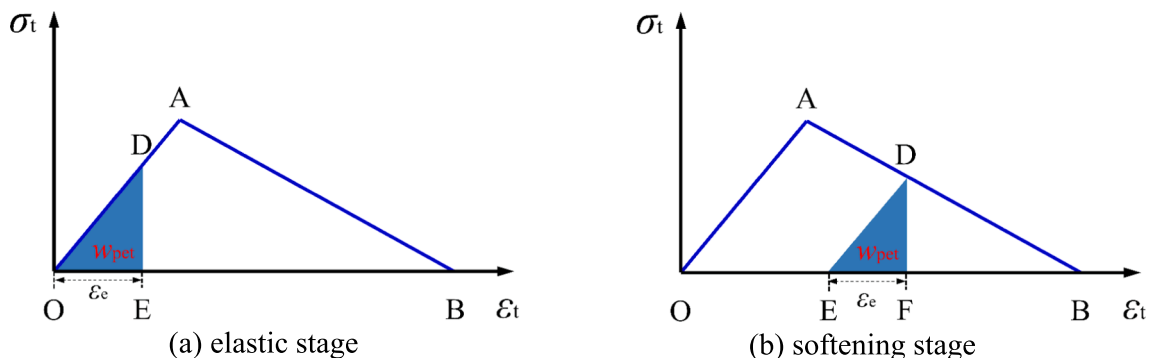

Fig. 5. Normal deformation energy w_{pet}.

(a) elastic stage

(b) softening stage
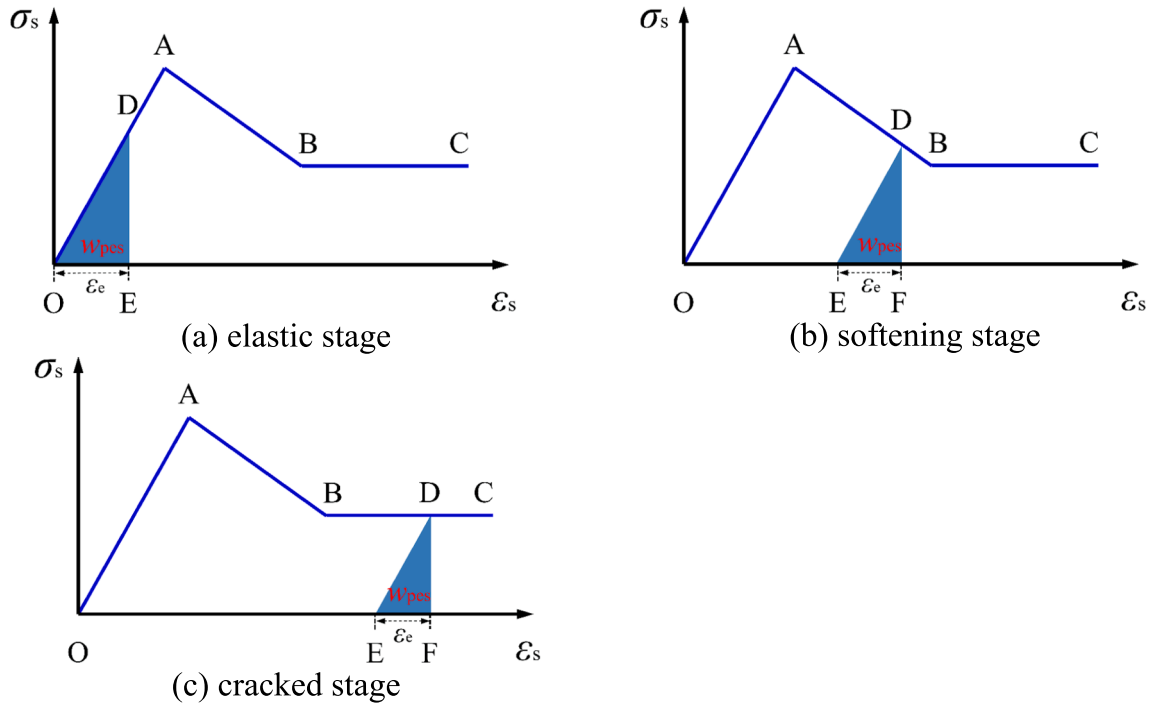

(c) cracked stage

Fig. 6. Tangential deformation energy w_{pes}.

enters the softening stage, σ_s and cohesion c_p decrease continuously, and it is determined that the spring undergoes shear damage. Once c_p decreases to zero, it is determined that the spring undergoes shear crack.

Based on the stress–strain curve of the bilinear cohesive fracture model, it is concluded that some energy will be dissipated once the spring undergoes damage, and the dissipation energy is defined as the fracture energy. Since there are differences in the statistical algorithm of spring fracture energy W_{PC} when the spring undergoes damage or crack, it is described separately.

(1) Damage status.

When the spring undergoes tensile damage, the normal stress is in the softening stage, and the area of quadrilateral OADE in Fig. 7 is equal to the tensile fracture energy w_{pct}, which is written as Eq. (23). When the spring undergoes shear damage, the tangential stress is in the softening stage, and the area of quadrilateral OADE in Fig. 8 is equal to the shear fracture energy w_{pcs}, which is written as Eq. (24).

$$w_{pct} = \left[\frac{1}{2}\sigma_{pt}\varepsilon_{td} - \frac{1}{2}\sigma_{pz}\left(\varepsilon_{td} - \left(\varepsilon_{pz} - \frac{\sigma_{pz}}{kn}\right)\right)\right]s_p \qquad (23)$$

where ε_{td} denotes the tensile cracked strain and ε_{pz} denotes the normal strain.
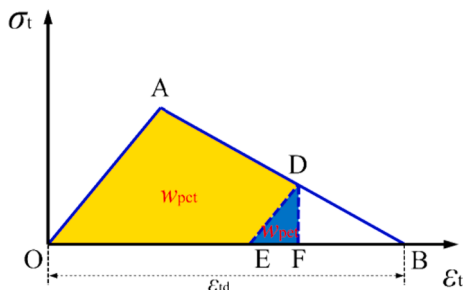

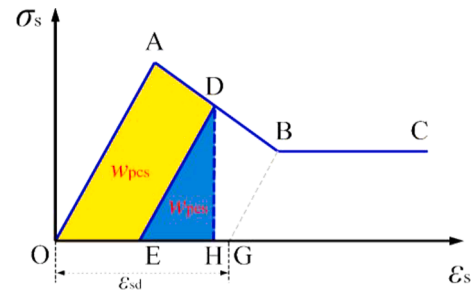**Fig. 7.** Tensile fracture energy w_{pct} for the tensile damage.

Fig. 8. Shear fracture energy w_{pcs} for the shear damage.

$$w_{pcs} = \left[\frac{1}{2}c_p\varepsilon_{sd} - \frac{1}{2}\left(\sigma_{ps} - \sigma_{pz}\tan\varphi\right)\left(\varepsilon_{sd} - \left(\varepsilon_{ps} - \frac{\sigma_{ps}}{k_s}\right)\right) + \sigma_{pz}\tan\varphi\left(\varepsilon_{ps} - \frac{\sigma_{ps}}{k_s}\right)\right]s_p$$

$$(24)$$

where ε_{sd} denotes the shear cracked strain and ε_{ps} denotes the resultant tangential strain.

(2) Cracked status

In the bilinear cohesive fracture model, when the tensile strength σ_{pt} becomes zero, the spring undergoes tensile fracture, and the cohesion c_p becomes zero accordingly. Therefore, when the spring undergoes tensile fracture, not only the tensile fracture energy w_{pct} but also the shear fracture energy w_{pcs} must be calculated. When c_p becomes zero, the numerical spring undergoes shear fracture, and σ_t also becomes zero. Therefore, when the spring undergoes shear fracture, not only the shear fracture energy w_{pcs} but also the tensile fracture energy w_{pct} must be calculated.

When the spring undergoes only tensile fracture, the area of triangle OAB in Fig. 9(c) is equal to w_{pct}. For the shear fracture energy w_{pcs}, there are differences in the calculation according to the tangential stress state.
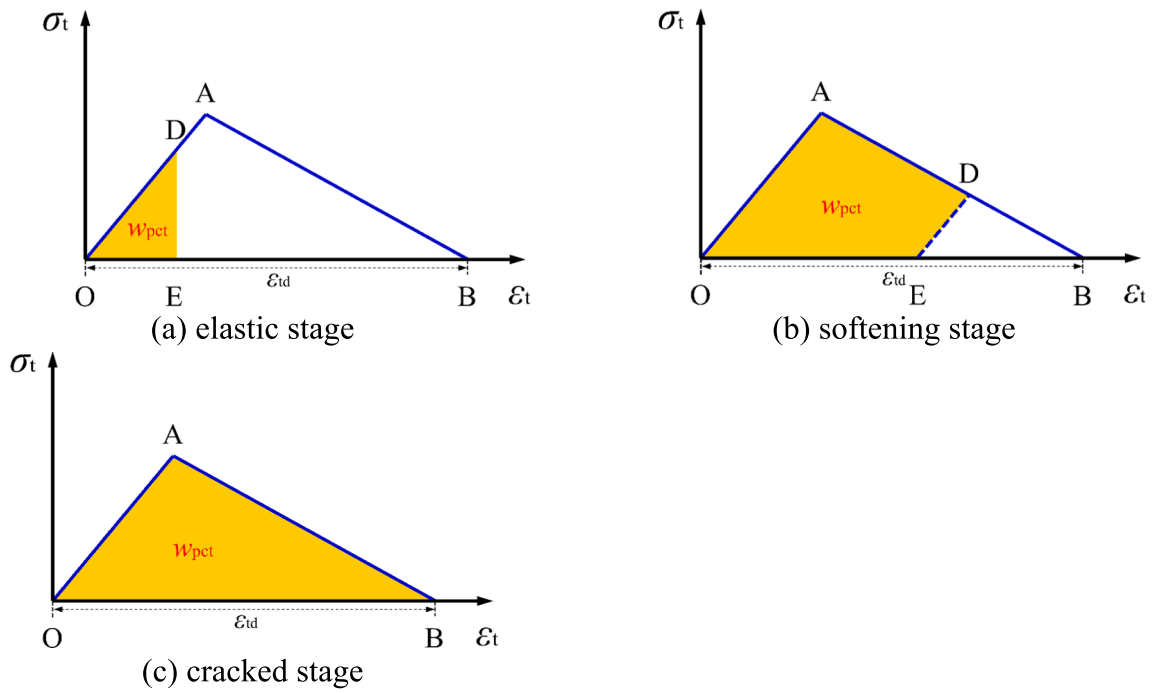
Fig. 9. Tensile fracture energy w_{pct}.

When the tangential stress corresponds to the elastic stage and the tangential stress is less than or equal to the sliding friction stress σ_{sd}, w_{pcs} is equal to zero. When the tangential stress corresponds to the elastic stage and is larger than σ_{sd}, the area of quadrilateral ODFE in Fig. 10(a) is equal to w_{pcs}. When the tangential stress corresponds to the softening stage, the area of pentagon OADFE in Fig. 10(b) is equal to w_{pcs}.

When the spring undergoes only shear fracture, the area of quadrilateral OABD in Fig. 10(c) is equal to w_{pcs}. For the tensile fracture energy w_{pct}, there are differences in the calculation according to the normal

stress state. When the normal stress is in compression, w_{pct} is equal to zero. When the normal spring is at the elastic stage of tension, the area of triangle ODE in Fig. 9(a) is equal to w_{pct}. When the normal stress corresponds to the softening stage of tension, the area of quadrilateral OADE in Fig. 9(b) is equal to w_{pct}.

When the spring undergoes combined tensile fracture and shear fracture, the area of triangle OAB in Fig. 9(c) is equal to w_{pct}, and the area of quadrilateral OABD in Fig. 10(c) is equal to w_{pcs}.

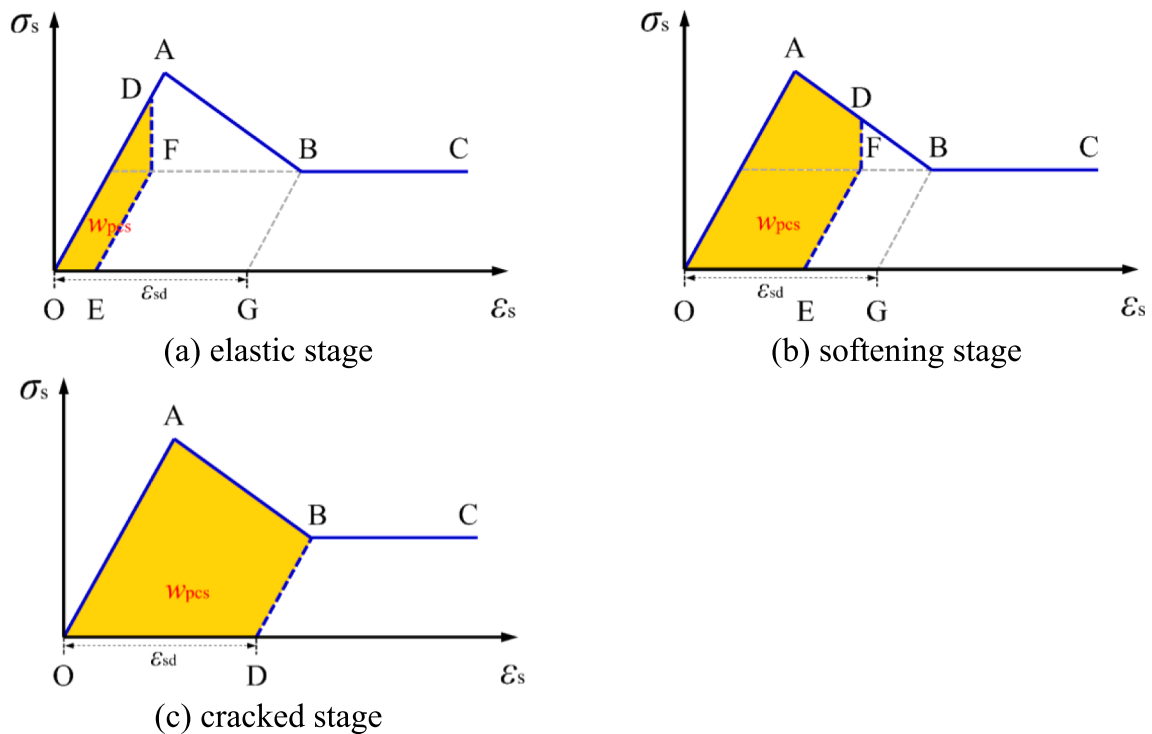To obtain the spring fracture energy W_{PC} of the entire model, first,

Fig. 10. Shear fracture energy w_{pcs}.

the tensile fracture energy w_{pct} is calculated based on Eq. (25). Second, the shear fracture energy w_{pcs} is calculated based on Eq. (26). Subsequently, the fracture energy w_{pc} of each cracked spring is calculated based on Eq. (27). Finally, all cracked springs are looped to obtain the spring fracture energy W_{PC} of the entire model (as shown in Eq. (28).

$$w_{pct} = \begin{cases} \dfrac{1}{2}\dfrac{\sigma_{pz}^2}{k_n}s_p & \text{Fig.9(a)} \\[2ex] \left[\dfrac{1}{2}\sigma_{pt}\varepsilon_{td} - \dfrac{1}{2}\sigma_{pz}\left(\varepsilon_{td} - \left(\varepsilon_{pz} - \dfrac{\sigma_{pz}}{kn}\right)\right)\right]s_p & \text{Fig.9(b)} \\[2ex] \dfrac{1}{2}\sigma_{pt}\varepsilon_{td}s_p & \text{Fig.9(c)} \end{cases} \tag{25}$$

$$w_{pcs} = \begin{cases} \left[\dfrac{1}{2}\dfrac{(\sigma_{ps} - \sigma_{pz}\tan\varphi)^2}{k_s} + \sigma_{pz}\tan\varphi\dfrac{(\sigma_{ps} - \sigma_{pz}\tan\varphi)}{k_s}\right]s_p & \text{Fig.10(a)} \\[3ex] \left[\dfrac{1}{2}c_p\varepsilon_{sd} - \dfrac{1}{2}(\sigma_{ps} - \sigma_{pz}\tan\varphi)\left(\varepsilon_{sd} - \left(\varepsilon_{ps} - \dfrac{\sigma_{pz}\tan\varphi}{k_s}\right)\right)\right. \\[2ex] \left. + \sigma_{pz}\tan\varphi\left(\varepsilon_{ps} - \dfrac{\sigma_{pz}\tan\varphi}{k_s}\right)\right]s_p & \text{Fig.10(b)} \\[2ex] \left(\dfrac{1}{2}c_p\varepsilon_{sd} + \sigma_{pz}\tan\varphi\varepsilon_{sd}\right)s_p & \text{Fig.10(c)} \end{cases}$$
$$\tag{26}$$

$$w_{pc} = w_{pct} + w_{pcs} \tag{27}$$

$$W_{PC} = \sum_{k=1}^{N_{pc}} w_{pc} \tag{28}$$

where N_{pc} denotes the number of cracked springs.

3.2.2.2. Unloading path.
For the normal stress of numerical spring, the tensile fracture energy w_{pct} during the unloading process is plotted in Fig. 11. At time t_i, the normal stress is located at point D. From t_i to t_{i+1}, the normal stress undergoes unloading, and it is located at point G at time t_{i+1}. The area of quadrilateral OADE in Fig. 11 is equal to the value of tensile fracture energy w_{pct}, which is defined as

$$w_{pct} = \frac{1}{2}(\sigma_{pt} + \sigma_{tm})\left(\varepsilon_{tm} - \frac{\sigma_{tm}}{kn}\right)s_p \tag{29}$$

where ε_{tm} denotes the tensile strain at point D and σ_{tm} denotes the tensile stress at point D.

For the tangential stress of numerical spring, the shear fracture energy w_{pcs} during the unloading process is plotted in Fig. 12. At time t_i, the tangential stress is located at point D. From t_i to t_{i+1}, the tangential stress undergoes unloading, and it is located at point G at time t_{i+1}. The area of quadrilateral OADE in Fig. 12 is equal to the value of shear fracture energy w_{pcs}, which is defined as

$$w_{pcs} = \frac{1}{2}(\sigma_{ps} + \sigma_{sm})\left(\varepsilon_{sm} - \frac{\sigma_{sm}}{k_t}\right)s_p \tag{30}$$

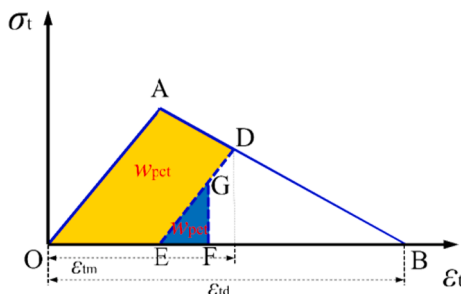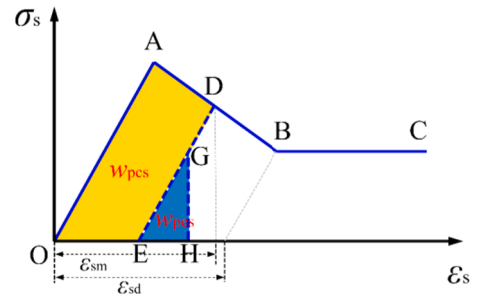**Fig. 11.** Tensile fracture energy w_{pct} during unloading.

Fig. 12. Shear fracture energy w_{pcs} during unloading.

where ε_{sm} denotes the tangential strain at point D and σ_{sm} denotes the tangential stress at point D.

3.2.3. Friction energy W_R
After the interface cracks, the blocks on both sides slide, which consumes some energy, and the friction energy W_R is only related to the tangential stress and tangential strain of numerical spring. The tangential state of spring at each time step is divided into a cracked state and uncracked state. Therefore, the state of spring from time t-Δt to time t includes four types: uncracked → uncracked, uncracked → cracked, cracked → uncracked and cracked → cracked. Considering both the tangential stress–strain curve and the interaction characteristics between blocks, it is concluded that the friction energy w_r is not zero only in the two cases of uncracked → cracked and cracked → cracked. When the tangential stress state of numerical spring changes from uncracked to cracked, the area of quadrilateral BDFE in Fig. 13(a) is equal to w_r. When the tangential stress state of numerical spring changes from cracked to cracked, the area of quadrilateral DHFE in Fig. 13(b) is equal to w_r. Since the CDEM adopts an explicit iterative algorithm, the relative friction displacement ΔU_i from time t-Δt to time t is written as

$$\Delta U_i = \begin{cases} 0 & \text{if } G_{t-\Delta t} = G_{uc}, G_t = G_{uc} \\[2ex] \left[\left(\varepsilon_{pi}^t - \dfrac{\sigma_{pi}^t}{k_s}\right) - \left(\varepsilon_{pi}^{t-\Delta t} - \dfrac{\sigma_{pi}^{t-\Delta t}}{k_s}\right)\right]l_{pi} & \text{if } G_{t-\Delta t} = G_{uc}, G_t = G_c \\[2ex] \left[\left(\varepsilon_{pi}^t - \dfrac{\sigma_{pi}^t}{k_s}\right) - \left(\varepsilon_{pi}^{t-\Delta t} - \dfrac{\sigma_{pi}^{t-\Delta t}}{k_s}\right)\right]l_{pi} & \text{if } G_{t-\Delta t} = G_c, G_t = G_c \\[2ex] 0 & \text{if } G_{t-\Delta t} = G_c, G_t = G_{uc} \end{cases}$$
$$\tag{31}$$

where $\varepsilon_{pi}^{t-\Delta t}$ and ε_{pi}^t denote the tangential strain components of numerical spring at time t-Δt and t, respectively. $\sigma_{pi}^{t-\Delta t}$ and σ_{pi}^t denote the tangential stress components of numerical spring at time t-Δt and t, respectively. l_{pi} denotes the characteristic length of numerical spring.

To calculate the friction energy W_R of the entire model, first, the relative friction displacement ΔU_i is calculated based on Eq. (31). Subsequently, the friction energy w_r of each numerical spring is calculated based on Eq. (32). Finally, all springs are looped to obtain the friction energy W_R of the entire model (as shown in Eq. (33).

$$w_r = \sigma_{px}s_p\Delta U_x + \sigma_{py}s_p\Delta U_y \tag{32}$$

$$W_R = \sum_{k=1}^{N_P} w_r \tag{33}$$

3.2.4. Gravitational potential energy W_G
The gravitational potential energy W_G is the energy that an object has because of the action of gravity, and the W_G of an object at a position in space is equal to the work done by gravity in moving the object from that position to a reference position. The gravitational potential energy W_G of the entire model is defined as
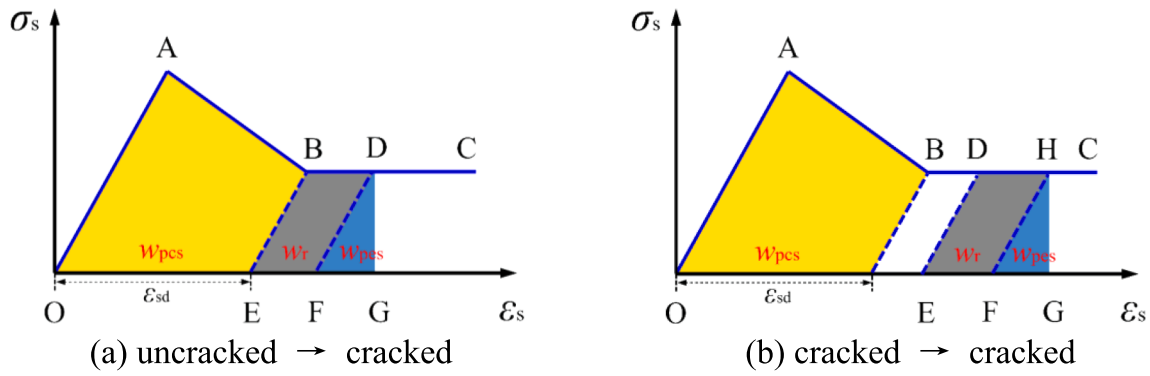
Fig. 13. Friction energy W_R.

$$W_G = \sum_{k=1}^{N_E} \rho v g h \tag{34}$$

where ρ denotes the element density. v denotes the element volume. g denotes the gravitational acceleration. h denotes the elevation of the element body centre relative to the reference position. N_e denotes the number of elements.

The change in gravitational potential energy ΔW_G is defined as

$$\Delta W_G = \sum_{k=1}^{N_E} \rho v g \Delta h \tag{35}$$

The calculation flow is plotted in Fig. 14. First, the acceleration, velocity and displacement of nodes are calculated. Subsequently, the deformation force of the elements and numerical springs is calculated, followed by obtaining the resultant force of the nodes. Then, the energy statistics algorithm is conducted to obtain the value of various energy components. Finally, the system calculation time is obtained, and it is determined whether to terminate the iterative calculation.

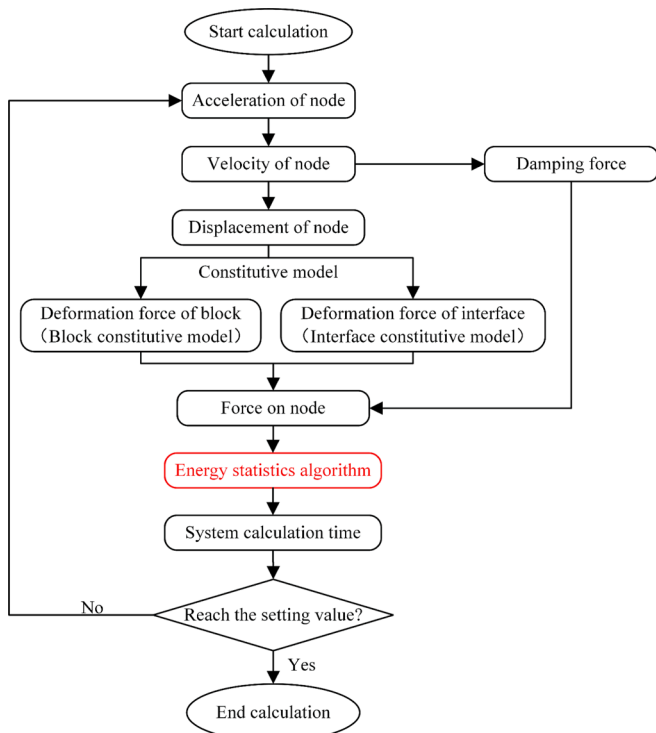In the energy statistics algorithm, there are many variables, some of

which are basic parameters of the numerical model (e.g., element number N_E, spring sectional area s_p), some of which are basic parameters of the bilinear cohesive fracture model (e.g., cohesion c_p, tensile strength σ_{pt}, friction angle φ), and some of which are process variables of the numerical simulation (e.g., spring normal stress σ_{pz}, spring tangential stress σ_{ps}, spring normal strain ε_{pz}, spring tangential strain ε_{ps}). When the energy statistics algorithm is introduced into the numerical simulation, no additional parameters need to be input. The researchers only need to set the constitutive model parameters of the material, and the energy statistical algorithm automatically reads the mechanical parameters to complete the computation of various energy components.

3.3. Verification

The accuracy of CDEM in simulating the mechanical response of material under static and dynamic loading has been verified by many scholars. Therefore, this section mainly investigates the accuracy and robustness of the energy statistics algorithm for the bilinear cohesive fracture model.

3.3.1. Uniaxial stretching test with a prefabricated groove

In the uniaxial stretching test with a prefabricated groove, the specimen mainly undergoes tensile fracture. To verify the accuracy of the energy statistics algorithm in the uniaxial stretching test with a prefabricated groove, a 3D numerical model is established (as shown in Fig. 15), with length $l = 50$ mm, height $h = 100$ mm, and thickness $d = 20$ mm. A groove is preset in the middle of the left side of the model, with width $w = 0.2$ mm and length $b = 12$ mm. The model is meshed with tetrahedral elements, with a total of 24,489 nodes and 126,675 elements. To simulate the fracture process of the specimen under uniaxial
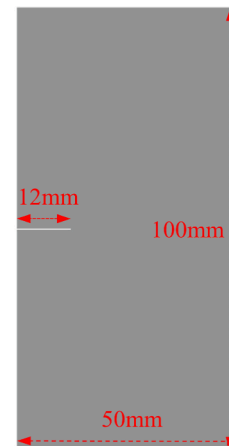

Fig. 14. Schematic diagram of the calculation flow in CDEM.

Fig. 15. Numerical model of the uniaxial stretching test with a prefabricated groove.

stretching conditions, vertical stretching displacement loading is applied at the top and bottom boundaries, and the loading velocity $v_y = 1 \times 10^{-9}$ m/s. During the numerical simulation of the uniaxial stretching test with a prefabricated groove, local nonviscous damping is adopted as the damping algorithm, and the value of the local damping coefficient α_L is set to 0.6. The mechanical parameters of the specimen are listed in Table 1. According to the energy conservation law, the cumulative value W_T of various energy components should be equal to the external work W_O made by the displacement loading.

The vertical displacement results of the specimen are plotted in Fig. 16. The crack expansion path at the outer surface of specimen is plotted in Fig. 17, and green indicates that the interface undergoes tensile fracture. The change curves of W_T and W_O are plotted in Fig. 18 (a). With increasing tensile strain, W_T and W_O continue to increase, and their change trends are basically the same. When the tensile strain ε_t reaches 0.8‰, the cumulative value of various energy components is $W_T = 8.37 \times 10^{-2}$ J, the external work is $W_O = 8.47 \times 10^{-2}$ J, and the error is $\gamma = 1.18\%$. The change curves of various energy components are plotted in Fig. 18(b). It can be concluded that the energy in the model is mainly the element deformation energy W_{EE} during the initial loading period. As the loading time increases, cracks gradually appear, and the element deformation energy W_{EE} gradually decreases. The spring fracture energy W_{PC} and damping energy W_D gradually increase.

Based on the corresponding relationship between W_O and W_T and the change trends of various energy components, the accuracy of the energy statistical algorithm in the uniaxial stretching test with a prefabricated groove is verified.

3.3.2. Uniaxial compression test with a hole

In the uniaxial compression test with a hole, the specimen undergoes tensile fracture, shear fracture and sliding friction. To verify the accuracy of the energy statistics algorithm in the uniaxial compression test with a hole, a 3D numerical model is established (as shown in Fig. 19), with length $l = 100$ mm, height $h = 100$ mm, and thickness $d = 50$ mm. A cylindrical hole with a diameter $d = 20$ mm is preset in the middle of the model. The model is meshed with tetrahedral elements, with a total of 12,622 nodes and 63,923 elements. To simulate the fracture process of the specimen under uniaxial compression conditions, a normal displacement constraint is applied at the bottom boundary, a vertical compression displacement loading is applied at the top boundary, and the loading velocity is $v_y = 1 \times 10^{-8}$ m/s. During the numerical simulation of the uniaxial compression test with a hole, local nonviscous damping is adopted as the damping algorithm, and the value of the local damping coefficient α_L is set to 0.8. The mechanical parameters are listed in Table 2. According to the energy conservation law, the cumulative value W_T of various energy components should be equal to the external work W_O made by the displacement loading.

The vertical displacement results of the specimen are plotted in Fig. 20. The crack expansion path at the outer surface of the specimen is plotted in Fig. 21. Green indicates that the interface undergoes tensile fracture, and red indicates that the interface undergoes shear fracture. The change curves of W_T and W_O are plotted in Fig. 22(a). It can be concluded that with increasing compressive strain, W_T and W_O continue to increase, and their change trends are basically the same. When the compressive strain ε_c reaches 5‰, the cumulative value of various energy components $W_T = 94.09$ J, the external work $W_O = 95.69$ J, and the error $\gamma = 1.67\%$. The change curves of various energy components are plotted in Fig. 22(b). It can be concluded that the energy in the model is mainly the element deformation energy W_{EE} during the initial loading

period and that the spring deformation energy W_{PE} also increases slowly. As the loading time increases, cracks gradually appear, and the element deformation energy W_{EE} and spring deformation energy W_{PE} gradually decrease. The spring fracture energy W_{PC}, friction energy W_R and damping energy W_D gradually increase.

Based on the corresponding relationship between W_O and W_T and the change trends of various energy components, the accuracy of the energy statistical algorithm in the uniaxial compression test with a hole is verified.

Based on the numerical results of the uniaxial stretching test and uniaxial compression test, not only the accuracy and robustness of the energy statistics algorithm for the bilinear cohesive fracture model but also the conservation of energy and mass of the CDEM during the initiation and propagation of cracks are verified. Therefore, the CDEM and energy statistics algorithm are adopted to conduct the full-time numerical simulation of rock mass under sequential detonation loading, and the displacement, fracture and energy evolution characteristics of the rock mass are investigated.

4. Numerical results

4.1. Basic background

4.1.1. Numerical model

The numerical model of the rock mass and explosives is plotted in Fig. 23, and the top boundary and left boundary of the model represent the ground. The horizontal length of the rock mass $l = 20$ m, the vertical height of the rock mass $h = 8$ m, and the diameter of the explosives $d = 0.025$ m. Three explosives are arranged at the same horizontal level with a vertical distance of 3 m from the top boundary, and the horizontal distance between adjacent explosives is 5 m. The model is meshed by triangular elements, with a total of 4270 nodes and 132,801 elements. To avoid stress wave reflection at the artificial truncation boundary, the right boundary and bottom boundary of the model are set as the reflection-free boundary.

Although local nonviscous damping was originally proposed to equilibrate static and quasistatic simulations, it has some advantages that make it attractive for dynamic simulations, and local nonviscous damping is adopted for the dynamic simulation in this study. According to the relationship between the local damping coefficient α_L and critical damping D, α_L is set to 0.001 in the dynamic simulation. Kuhlemeyer and Lysmer (1973) proposed that for the accurate simulation of wave transmission, the element size Δl must be smaller than $1/10 \sim 1/8$ of the wavelength associated with the highest frequency component of the wave. Considering the computational efficiency and the influence of the mesh size on the high-frequency component dispersion, the mesh of the explosives and rock mass around the explosives is refined, and this mesh size is set to 0.01 m. As the distance from the explosive increases, the mesh size of the rock mass gradually increases to a maximum mesh size of 0.2 m, which is sufficient to accurately describe the wave transmission.

4.1.2. Mechanical parameters

The Jones-Wilkins-Lee (JWL) equation of state is adopted to simulate the explosive initiation process. The equation of state was proposed by Lee in 1965 based on the work of Jones and Wilkins and is written as

$$P = A\left(1 - \frac{\omega}{R_1 V'}\right)e^{-R_1 V'} + B\left(1 - \frac{\omega}{R_2 V'}\right)e^{-R_2 V'} + \frac{\omega E_0}{V'} \quad (36)$$

where P denotes the instantaneous pressure of detonation products, V' denotes the relative volume of detonation products, and E_0 denotes the specific internal energy of detonation products at the initial moment. A, B, R_1, and R_2 are obtained from the cylindrical test.

The type of explosive simulated in the paper is TNT, and the JWL parameters of TNT derived from Liu (Liu et al., 2022) are listed in
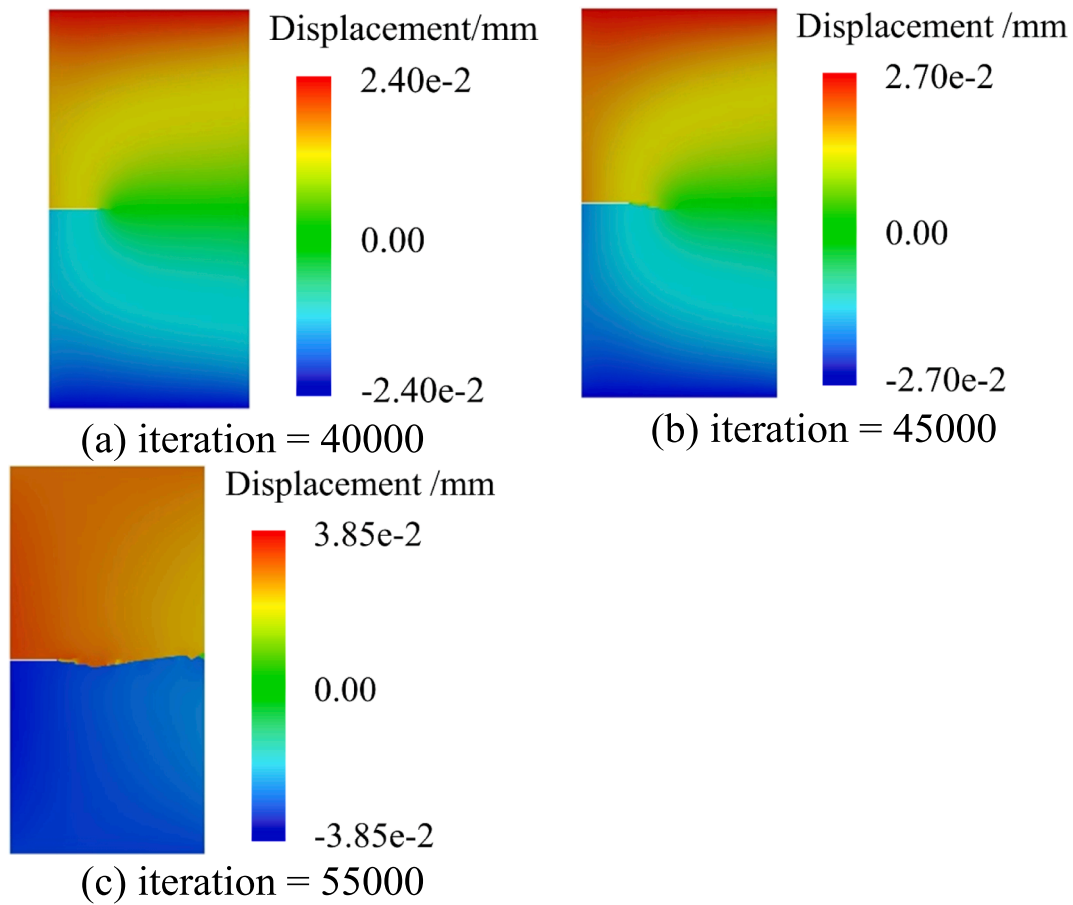
Table 1
Mechanical parameters of the specimen.

Density(kg/ m³)	Elastic modulus (GPa)	Cohesion (MPa)	Tensile strength (MPa)	Friction angle(°)
2300	5	8	5	35

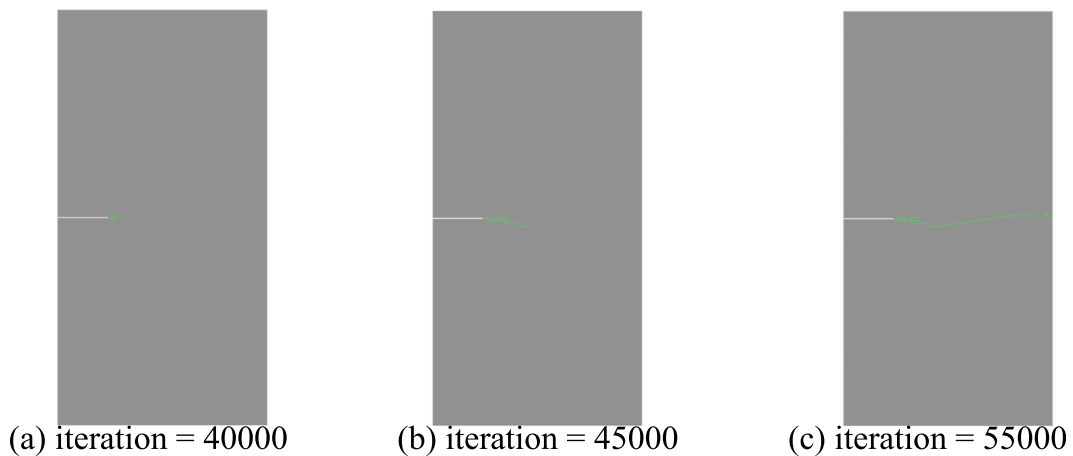**Fig. 16.** Vertical displacement nephograms.

Fig. 17. Crack expansion path at the outer surface of the specimen.

Table 3. To simulate the sequential detonation process, the initiation time interval t_g between explosives is set to 0.03 s, and the mechanical parameters of the rock mass are listed in Table 4.

4.2. Displacement characteristics

4.2.1. Resultant displacement results

The resultant displacement nephograms of the rock mass under sequential detonation loading at different moments are plotted in Fig. 24. $t = 0.00$ s, $t = 0.03$ s and $t = 0.06$ s indicate the start times of the first explosion, second explosion and third explosion, respectively. $t =$

0.01 s, $t = 0.04$ s and $t = 0.07$ s indicate the end times of the first explosion, second explosion and third explosion, respectively.

At the end of the first explosion (Fig. 24(a)), the rock in the triangular area on the left side is significantly deformed and slightly slipped under the action of the explosion gas. There are two funnel-shaped areas (the yellow areas in Fig. 24(a)) where the rock has a larger displacement than that in the surrounding area; one funnel-shaped area is located between explosive 1 and the left boundary, and the other funnel-shaped area is located between explosive 1 and the top boundary. Although the explosion gas of explosive 1 disappears, the slipped rock has a larger movement velocity, and the displacement of rock in the triangle area
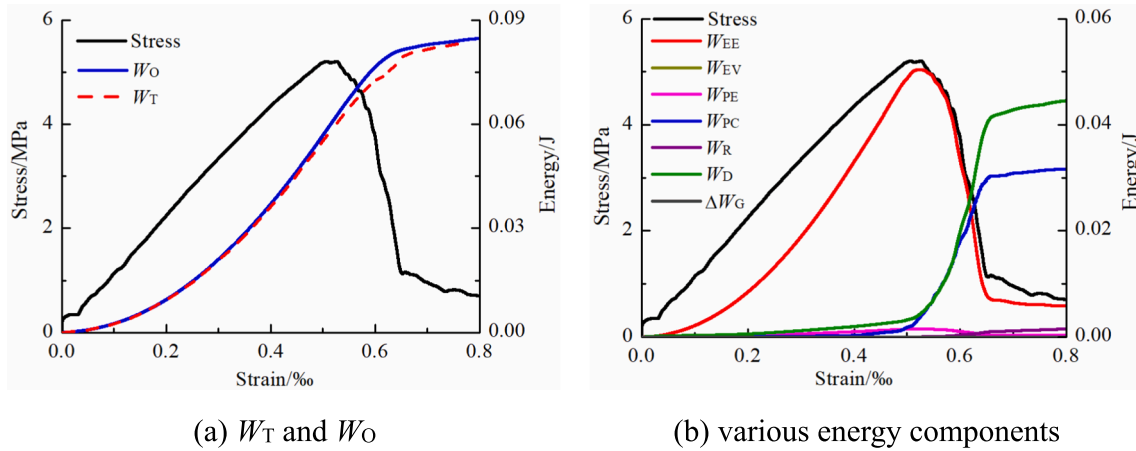
(a) W_T and W_O

(b) various energy components

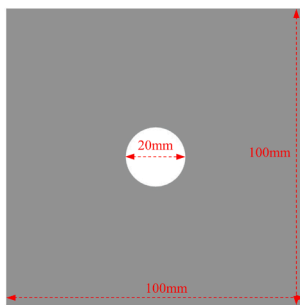**Fig. 18.** Change curves of stress and energy in the uniaxial stretching test.

Fig. 19. Numerical model of the uniaxial compression test with a hole.

Table 2
Mechanical parameters of the specimen.

Density(kg/ m³)	Elastic modulus (GPa)	Cohesion (MPa)	Tensile strength (MPa)	Friction angle(°)
2630	24.7	29	7.19	30

continues to increase from $t = 0.01$ s to $t = 0.03$ s. By the start time of the second explosion (Fig. 24(b)), the rock in the triangular area has experienced significant slippage, and the increase in displacement of the funnel-shaped area is larger than that of the surrounding area.

Under the action of the explosion gas of explosive 2, the rock above explosive 2 also slips, and the newly emerging slippage area is connected to the slippage area generated by explosive 1 at the end time of the second explosion (Fig. 24(c)). At the start time of the third explosion (Fig. 24(d)), the rock on the left of explosion 1 and above explosive 1 is significantly scattered, and the rock above explosive 2 also slips obviously.

At the end of the third explosion (Fig. 24(e)), the scattering phenomenon of rock above and on the left of explosive 1 becomes more significant, the displacement of rock above explosive 2 also continues to increase, and the rock above explosive 3 slips slightly. By $t = 0.1$ s (Fig. 24(f)), the rock above explosive 3 has obviously slipped, and the scattering phenomenon of rock above explosive 1, on the left of explosive 1 and above explosive 2 becomes more obvious.

4.2.2. Resultant displacement curve

The resultant displacement curves at the left boundary are plotted in Fig. 25. The displacement at the same position continues to increase with increasing time. For the same moment, the displacement first increases and then decreases with increasing y because the distance between the monitoring point and explosives first decreases and then

increases with increasing y. When the distance between the monitoring point and explosives decreases, the detonation loading that the rock bears increases, resulting in larger deformation and displacement. In addition, the value of y corresponding to the maximum displacement is larger than the value of y corresponding to the explosive because of the overlying rock weight.

The resultant displacement curves at the top boundary are plotted in Fig. 26. Within the first 0.07 s, the displacement first increases and then decreases with increasing ×, and the value of × corresponding to the maximum displacement is approximately equal to the value of × corresponding to explosive 1. When the time $t = 0.1$ s, there are three inflection points on the curve, and the values of × corresponding to the first, second and third inflection points are approximately equal to the value of × corresponding to explosions 1, 2 and 3, respectively. During the initial period, although the detonation loading of explosives 2 and 3 has an influence on the acceleration of the rock mass, the influence on the displacement is negligible. With increasing time, the influence on the displacement gradually becomes obvious, and three inflection points appear.

4.3. Fracture characteristics

4.3.1. Fracture ratio α

To quantitatively study the fracture evolution characteristics of the rock mass under sequential detonation loading, a dimensionless quantity, the fracture ratio α, is introduced:

$$\alpha = \frac{S_c}{S_a} \tag{37}$$

where α denotes the fracture ratio. S_c denotes the area of the cracked interface. S_a denotes the area of all interfaces.

The time-history curve of fracture ratio α is plotted in Fig. 27. Periods A, C and E represent the first, second, and third explosion periods, respectively; Periods B, D and F represent the first, second, and third post-explosion periods, respectively. The fracture ratio α gradually increases with increasing time, and the time-history curve of α has an obvious staged characteristic, which is closely related to the characteristics of the explosives. During the explosion periods, α increases sharply, and the rate of increase is not constant. At the beginning of the explosion period, α increases rapidly, and then the rate of increase gradually decays, which is due to the gradual reduction in explosion gas pressure. During the post-explosion periods, α increases slowly and ultimately no longer changes because of the disappearance of explosion gas. At the end of the first explosion period, the fracture ratio $\alpha_a = 14.49\%$. At the end of the second explosion period, the fracture ratio $\alpha_c = 33.13\%$. At the end of the third explosion, the fracture ratio $\alpha_e =$
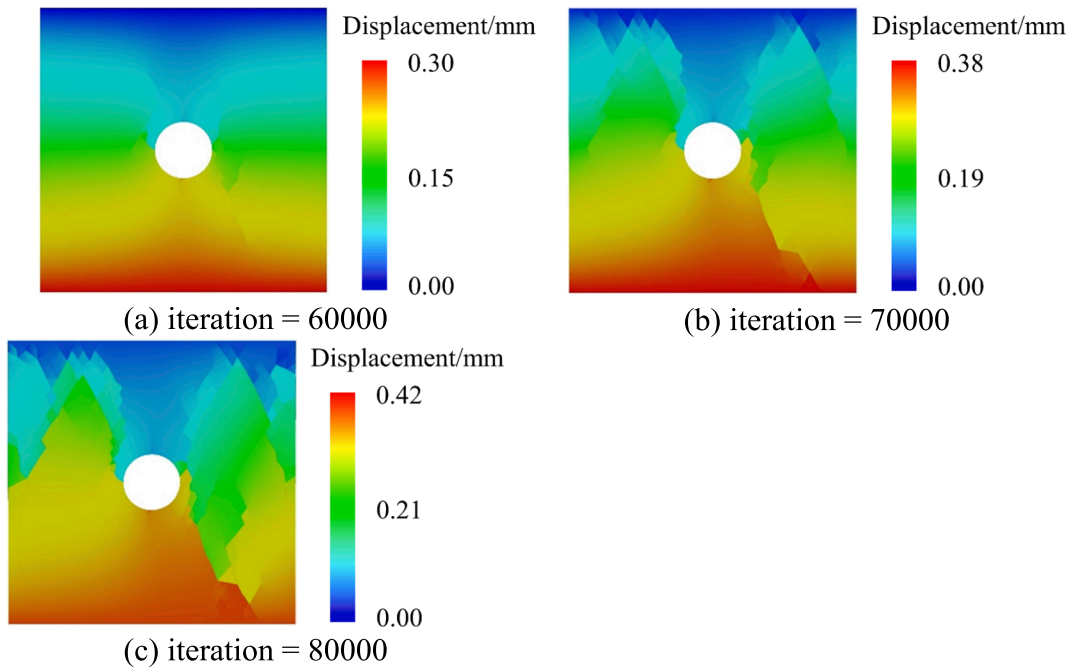
(a) iteration = 60000

(b) iteration = 70000

(c) iteration = 80000

Fig. 20. Vertical displacement nephograms.

(a) iteration = 60000

(b) iteration = 70000

(c) iteration = 80000
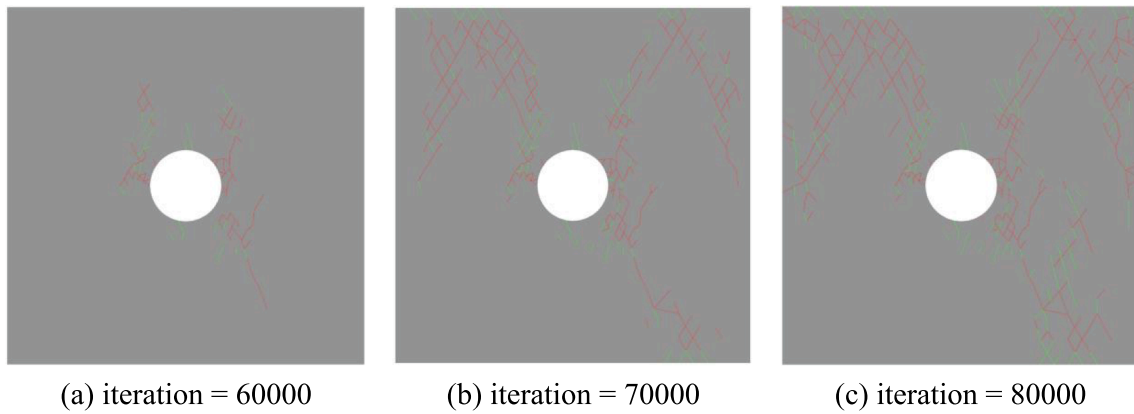
Fig. 21. Crack expansion paths at the outer surface of the specimen.

(a) W_T and W_O

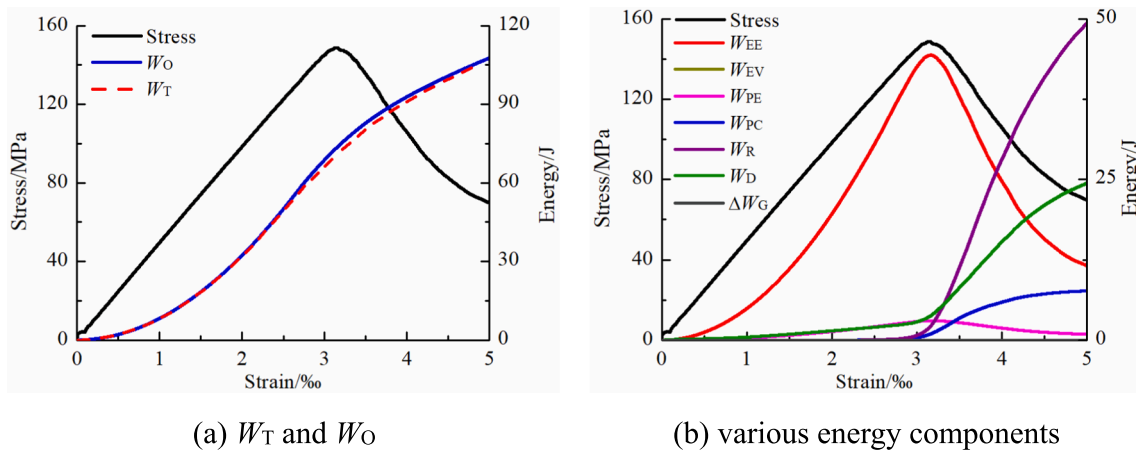(b) various energy components

Fig. 22. Change curves of stress and energy in the uniaxial compression test.
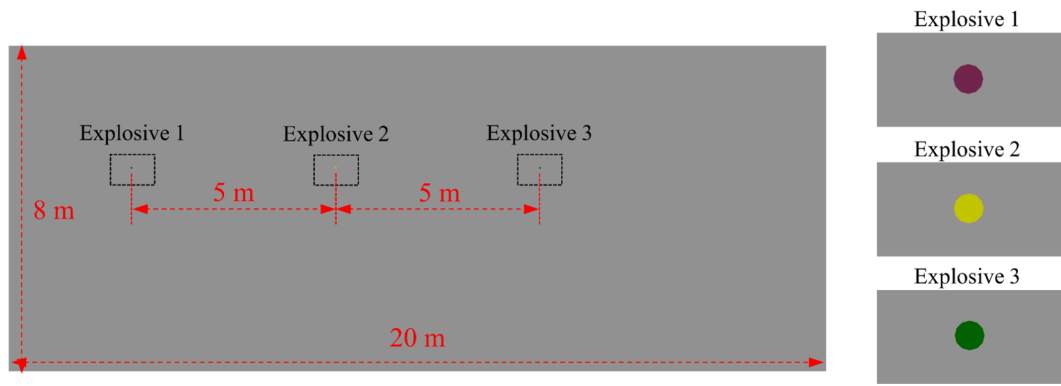
Fig. 23. Numerical model of the rock mass and explosives.

Table 3
JWL parameters of TNT.

Charge density (kg/m³)	Initial internal energy (J/m³)	CJ pressure (Pa)	Detonation velocity (m/s)
1630	7e9	21e9	6930

Table 4
Mechanical parameters of the rock mass.

Density (kg/m³)	Elastic modulus(GPa)	Cohesion strength(MPa)	Tensile strength(MPa)	Friction angle(°)
2500	50	6	2	40

48.81%. It can be concluded that fracture ratio α increases the most during the second explosion period. This is due to the appearance of new free faces after the first explosion, and some interfaces have been damaged but not fractured, which are then easily fractured under detonation loading during the second explosion period.

4.3.2. Initial fracture results

To further investigate the fracture type and spatial distribution characteristics of cracked interfaces, the initial fracture nephograms of interfaces are plotted in Fig. 28. The green line indicates that the interface undergoes tensile fracture, and the red line indicates that the interface undergoes shear fracture. At the end of the first explosion (Fig. 28(a)), the cracked interfaces are mainly near explosive 1, and the interfaces near explosive 1 and the top boundary mainly undergo shear fracture. As the distance from explosive 1 increases, the proportion of interfaces that undergo tensile fracture gradually increases. From $t =$
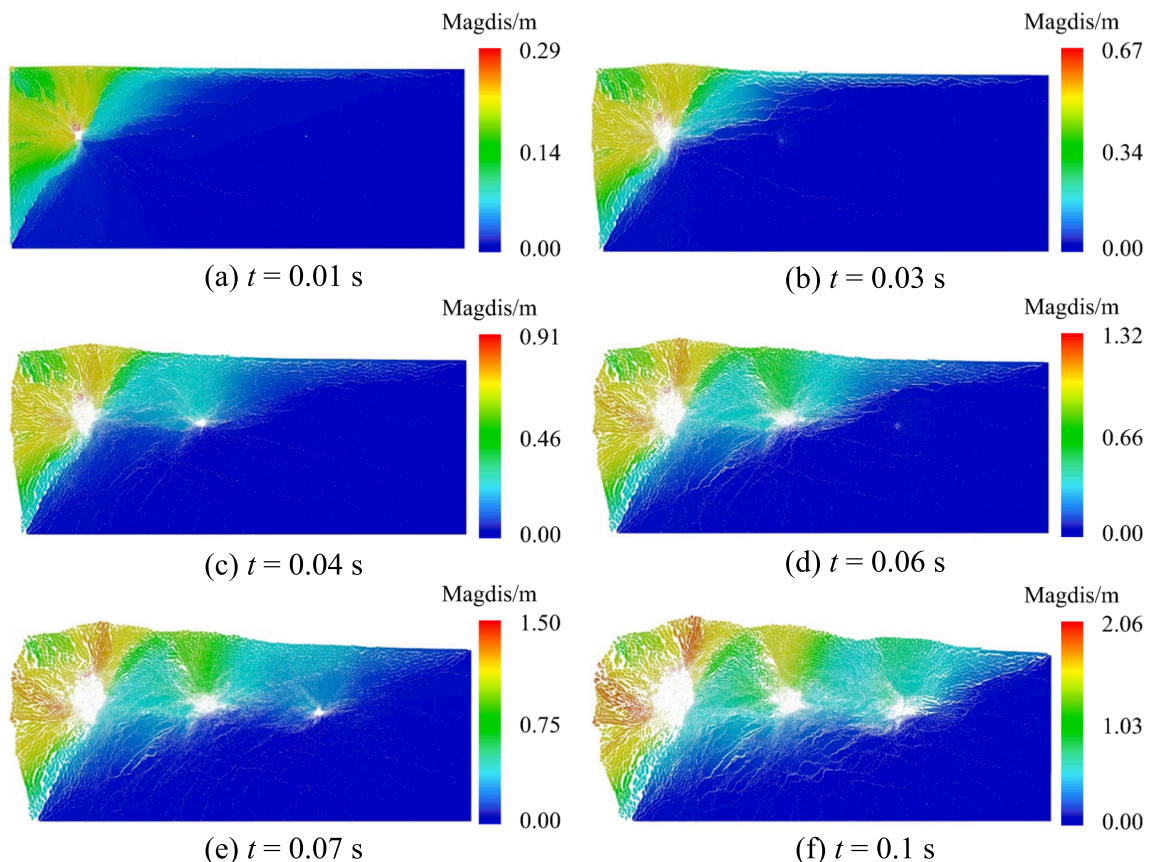

(a) $t = 0.01$ s

(b) $t = 0.03$ s

(c) $t = 0.04$ s

(d) $t = 0.06$ s

(e) $t = 0.07$ s

(f) $t = 0.1$ s

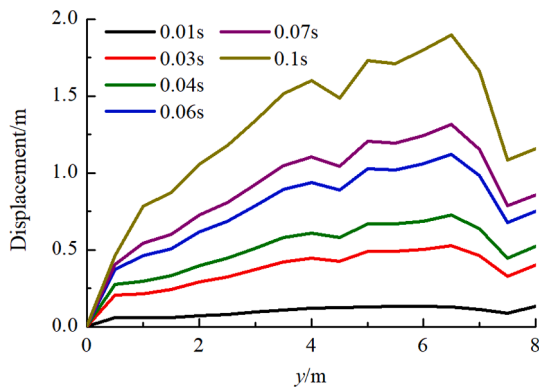**Fig. 24.** Resultant displacement nephograms of the rock mass.

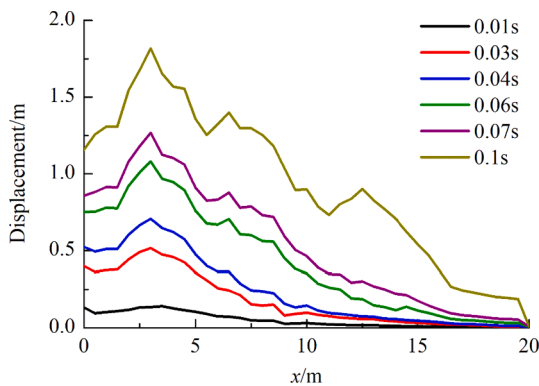**Fig. 25.** Displacement curves at left boundary.
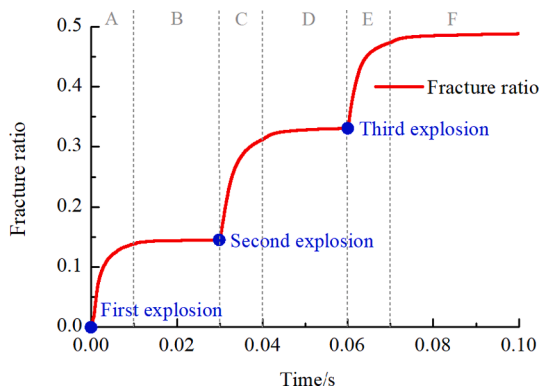

Fig. 26. Displacement curves at top boundary.

Fig. 27. Time-history curve of fracture ratio α.

0.01 s to $t = 0.03$ s (Fig. 28(b)), there are still a few interfaces that undergo tensile fracture and shear fracture. At the end of the second explosion (Fig. 28(c)), the newly cracked interfaces are mainly near explosive 2, and compared to explosive 1, the proportion of the interface undergoing tensile fracture around explosive 2 significantly increases. As the distance from explosive 2 increases, the proportion of interfaces that undergo tensile fracture gradually increases. From $t = 0.04$ s to $t = 0.06$ s (Fig. 28(d)), there are still a few interfaces that undergo tensile and shear fracture. Since the tensile fracture energy and tensile strength are much less than the shear fracture energy and shear strength, the newly cracked interfaces mainly undergo tensile fracture. At the end of the third explosion (Fig. 28(e)), the newly cracked interfaces are mainly near explosive 3, and the interfaces near explosive 3 mainly undergo tensile fracture. By time $t = 0.1$ s (Fig. 28(f)), the fracture nephogram no longer changes. Based on the fracture nephograms at different moments,

the fracture type and the spatial distribution characteristics of cracked interfaces are closely related to the characteristics of explosives 1, 2 and 3.

4.4. Energy characteristics

4.4.1. Element energy W_{EE} and W_{EV}

The time-history curve of element deformation energy W_{EE} is plotted in Fig. 29(a), and it is observed that the time-history curve has an obvious staged characteristic. During the explosion periods of explosions 1, 2 and 3, the change trends of W_{EE} are similar. However, there is a significant difference in the change trends between the explosion period and the post-explosion period. At the beginning of the explosion period, W_{EE} increases sharply to the maximum value due to the high explosion gas pressure. Subsequently, W_{EE} decreases sharply due to the reduction in explosion gas pressure and the interaction between elements, including fracture and slippage. At the beginning of the post-explosion period, the external force applied at the elements decreases sharply due to the disappearance of explosion gas, resulting in a sharp decrease in the element deformation energy W_{EE}, and then the decreasing trend decays. The maximum values of W_{EE} during the three explosion periods are basically the same, which indicates that the fracture and movement of the rock mass caused by the previous explosion do not have a significant influence on the maximum value of W_{EE}.

The time-history curve of element kinetic energy W_{EV} is plotted in Fig. 29(b), and it is observed that the time-history curve has an obvious staged characteristic. During the explosion periods of explosions 1, 2 and 3, the change trends of W_{EV} are similar. However, there is a significant difference in the change trends between the explosion period and the post-explosion period. At the beginning of the explosion period, the element acceleration is large due to the high explosion gas pressure, which results in a sharp increase in W_{EV}. Subsequently, with the reduction in explosion gas pressure, the force exerted by the explosion gas on the elements gradually decreases, and the element acceleration gradually decreases, which results in a decrease in the rate of increase in W_{EV}. During the post-explosion period, W_{EV} gradually decreases due to gravity and the interaction between elements. W_{EV} increases the most during the first explosion period, and the increase in W_{EV} during the explosion periods gradually decreases with increasing time.

4.4.2. Spring energy W_{PE} and W_{PC}

The time-history curve of the spring deformation energy W_{PE} is plotted in Fig. 29(c). The change trends of W_{PE} at the beginning stage of the three explosion periods are similar, but there are a few differences in the change trend during the three explosion periods at the later stage. In addition, there is a significant difference in the change trends between the explosion period and the post-explosion period. At the beginning of the explosion period, the squeezing and slippage between the elements near the explosive cause the normal stress and tangential stress of the numerical springs to increase sharply, so W_{PE} increases sharply to the maximum value. As the explosion gas pressure decays, the squeezing and slippage between the elements are weakened, resulting in a rapid decrease in W_{PE}. However, since the rock far from the explosive has not yet been significantly displaced, when the rock near the explosive moves to the outside, squeezing and slippage between the elements occur again, so W_{PE} fluctuates during the three explosion periods at the later stage. When the explosion gas disappears, the interaction between the elements is significantly weakened, resulting in a sharp decrease in W_{PE}, followed by a gradual decrease.

The time-history curve of the spring fracture energy W_{PC} is plotted in Fig. 29(d), and it is observed that the time-history curve has an obvious staged characteristic. During the explosion periods of explosives 1, 2 and 3, the change trends of W_{PC} are similar. However, there is a significant difference in the change trends between the explosion period and the post-explosion period. According to Eq. (23) to Eq. (30), the change trend of W_{PC} is closely related to the change trend of the cracked area S_c.

(a) $t = 0.01$ s

(b) $t = 0.03$ s

(c) $t = 0.04$ s
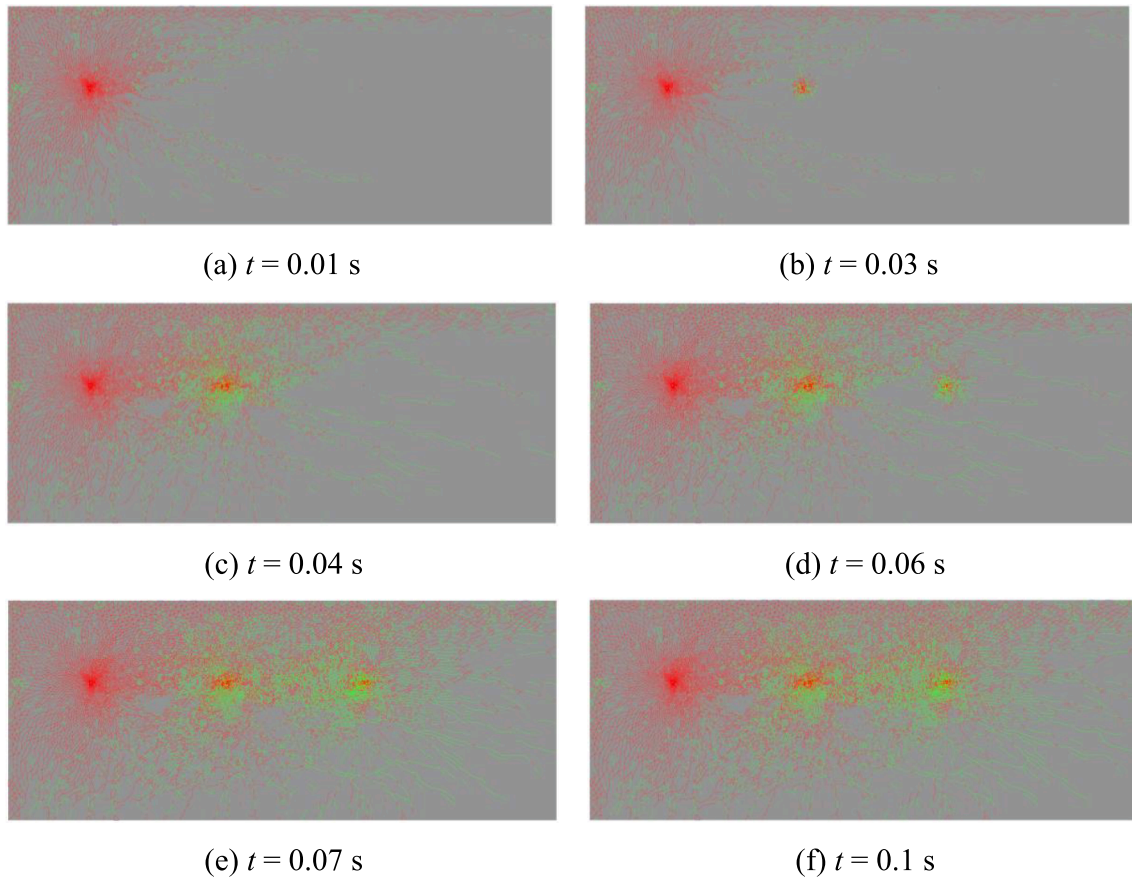
(d) $t = 0.06$ s

(e) $t = 0.07$ s

(f) $t = 0.1$ s

Fig. 28. Initial fracture nephograms of interfaces.

At the beginning of the explosion period, many interfaces satisfy the fracture criterion and become cracked, so W_{PC} increases sharply. Subsequently, as the explosion gas pressure decreases, the increase in stress at the interface decays, which leads to a gradual decrease in the increase in S_c, so the increase in W_{PC} also gradually decays. After the explosion gas disappears, the stress at some interfaces continues to increase, the fracture criterion is satisfied, and the interface cracks, so W_{PC} slowly increases. Finally, no interface satisfies the fracture criterion, and W_{PC} no longer increases. Until the next explosion happens, many interfaces crack, causing W_{PC} to increase sharply again.

4.4.3. Dissipated energy W_R and W_D

The time-history curve of friction energy W_R is plotted in Fig. 29(e), and it is observed that the time-history curve has an obvious staged characteristic. During the explosion periods of explosives 1, 2 and 3, the change trends of W_R are similar. However, there is a significant difference in the change trends between the explosion period and the post-explosion period. According to Eq. (31), W_R only occurs at the cracked interface, so its increasing trend is closely related to that of cracked area S_c. At the beginning of the explosion period, many interfaces satisfy the fracture criterion and become cracked due to the high explosion gas pressure. Sliding friction occurs between the elements on both sides of the cracked interface, so W_R increases sharply. Subsequently, as the explosion gas pressure decreases, the increase in S_c decays, which leads to a gradual decrease in the increase in W_R. During the post-explosion period, the elements on both sides of the cracked interface still undergo sliding friction, so W_R increases slowly.

The time-history curve of damping energy W_D is plotted in Fig. 29(f), and it is observed that the time-history curve has an obvious staged characteristic. During the explosion periods of explosions 1, 2 and 3, the change trends of W_D are similar. However, there is a significant

difference in the change trends between the explosion period and the post-explosion period. According to the formula of W_D, W_D is only related to the damping coefficient, nodal force and displacement increment, and the damping coefficient is constant. At the beginning of the explosion period, the nodal force is large because of the high explosion gas pressure. Although the displacement increment is small, W_D still increases sharply. Along with the decay of explosion gas pressure, the nodal force gradually decreases, resulting in a gradual decrease in the increase in W_D. Although the explosion gas disappears in the post-explosion period, the nodal force and displacement increment are not zero, resulting in a slow increase in W_D. By comparing the increase in W_D among the different post-detonation periods, it is concluded that as the time of explosions increases, the increase in W_D gradually increases.

4.4.4. Gravitational energy ΔW_G

The time-history curve of the change ΔW_G in gravitational potential energy is plotted in Fig. 29(g). The change trends of ΔW_G during the explosion period and post-explosion period are similar, and the increase in ΔW_G during the explosion period gradually increases as the time of explosion increases. Based on Eq. (35), the value of ΔW_G is only related to the gravitational acceleration, mass and vertical displacement increment. Since the gravitational acceleration and mass do not change, the change trend of ΔW_G is only determined by the vertical displacement increment. During the explosion period, the vertical displacement increment is larger than zero because of the action of the explosion gas, so ΔW_G gradually increases. Since the vertical acceleration of the rock mass is positive, the vertical velocity and displacement increment gradually increase, resulting in the rate of increase in ΔW_G gradually increasing. During the post-explosion period, the rock elements still move upwards, and ΔW_G gradually increases. However, due to the influence of gravity and the interaction between elements, the vertical
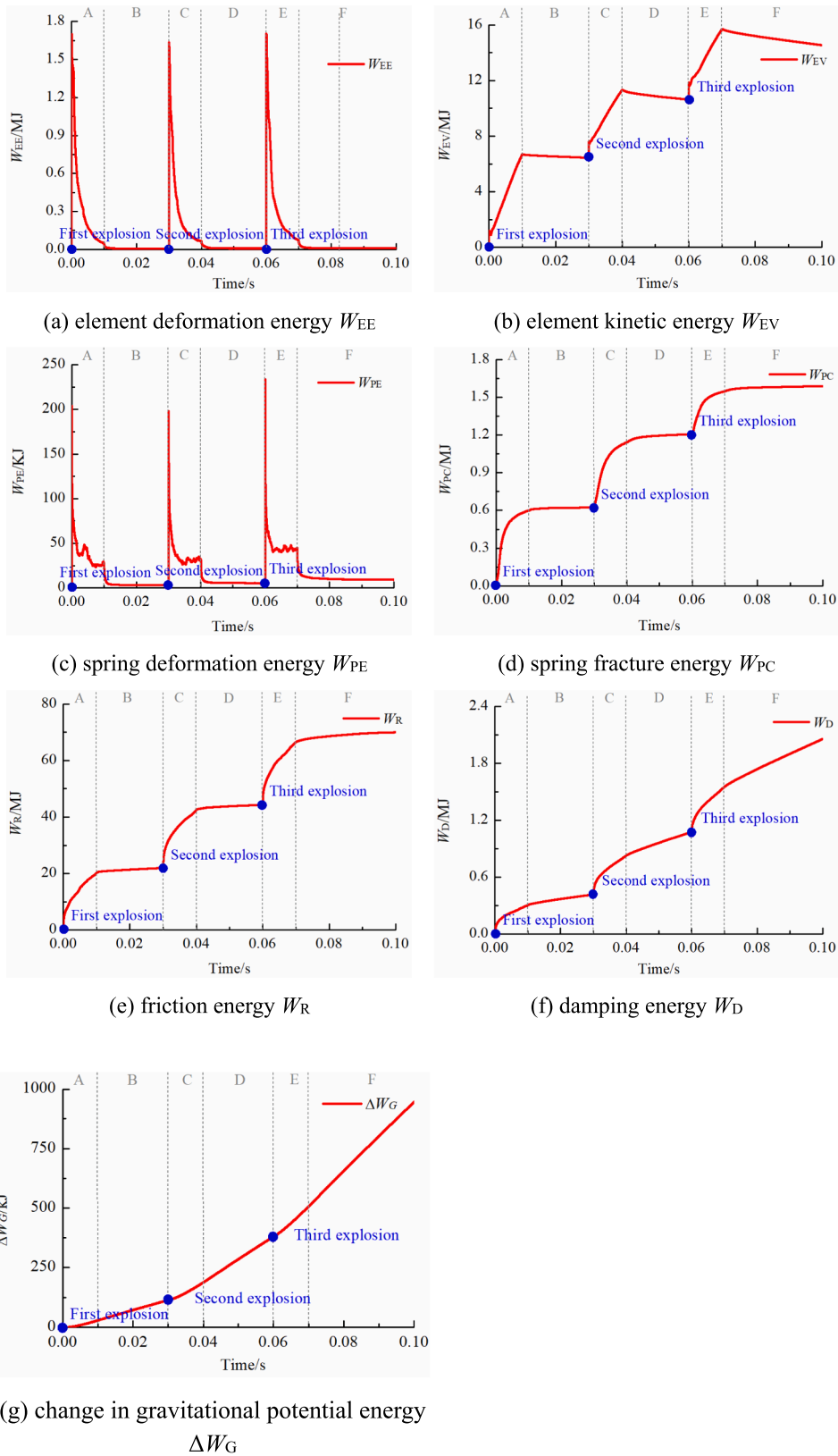
(a) element deformation energy W_{EE}

(b) element kinetic energy W_{EV}

(c) spring deformation energy W_{PE}

(d) spring fracture energy W_{PC}

(e) friction energy W_{R}

(f) damping energy W_{D}

(g) change in gravitational potential energy ΔW_{G}

Fig. 29. Time-history curves of various energy components.

velocity gradually decreases, and the rate of increase in ΔW_{G} is smaller than that during the explosion period. In addition, with the increase in the time of explosions, the rate of increase in ΔW_{G} during the post-explosion period gradually increases.

5. Conclusions

To optimize the control parameters of multiple-hole blasting, reduce the detrimental effect on surrounding facilities and improve the

utilization efficiency of explosion energy, the dynamic mechanical responses of rock mass under sequential explosive detonation, including the displacement, fracture and energy evolution characteristics, are investigated in this study. Based on the rock fracture status and the stress–strain curve of the bilinear cohesive fracture model, an energy statistics algorithm considering all energy components is first proposed, and the accuracy and robustness are verified. Then, the CDEM and energy statistics algorithm are adopted to simulate the dynamic response of rock mass under sequential detonation loading, and a dimensionless index, the fracture ratio α, is introduced to quantitatively analyse the change trend of the cracked interface. The results indicate that the CDEM and energy statistics algorithm can accurately model the dynamic response of rock mass under sequential detonation loading and obtain the complex conversion process of explosion energy in the rock mass. The following conclusions can be drawn:

1) The weight of the overlying rock mass affects the spatial distribution of displacement at the free face. For the top free face, the horizontal position corresponding to the maximum displacement is equal to the horizontal position of explosive 1. However, for the left free face, the vertical position corresponding to the maximum displacement is higher than the vertical position of the explosives.
2) The cracked interface mainly appears during the explosion periods, and the cracked interface generated by explosive 2 is largest because of the new free face caused by explosive 1. The damage on the interface caused by the previous explosion has a significant effect on the fracture type; the rock around explosive 1 mainly undergoes shear fracture, while the rock around explosives 2 and 3 mainly undergoes tensile fracture.
3) The change trends of various energy components are different during the explosion periods and post-explosion periods, which is closely related to the dynamic response of the rock mass. The explosion energy is mainly converted into friction energy W_R and element kinetic energy W_{EV}, and only a small proportion of explosion energy is used to break the rock mass.

CRediT authorship contribution statement

Qindong Lin: Conceptualization, Methodology, Writing – original draft, Writing – review & editing. **Xinguang Zhu:** Writing – review & editing, Formal analysis, Supervision. **Jianfei Yuan:** Investigation, Conceptualization, Validation. **Chun Feng:** Software, Visualization, Supervision. **Yundan Gan:** Investigation, Data curation. **Wenjun Jiao:** Data curation, Writing – review & editing. **Yulei Zhang:** Investigation.

Declaration of Competing Interest

The authors declare that they have no known competing financial interests or personal relationships that could have appeared to influence the work reported in this paper.

Data availability

Data will be made available on request.

References

Abdollahipour, A., Marji, M.F., 2020. A thermo-hydromechanical displacement discontinuity method to model fractures in high-pressure, high-temperature environments. Renew. Energ. 153, 1488–1530.
Abdollahipour, A., Marji, M.F., Bafghi, A.Y., Gholamnejad, J., 2016. Time-dependent crack propagation in a poroelastic medium using a fully coupled hydromechanical displacement discontinuity method. Int. F. Fract. 199 (1), 71–87.
Ai, Z.Y., Chen, Y.F., 2020. FEM-BEM coupling analysis of vertically loaded rock-socketed pile in multilayered transversely isotropic saturated media. Comput. Geotech. 120, 103437.
Alizadeh, R., Marji, M.F., Abdollahipour, A., Sagand, M.P., 2023. Numerical simulation of fatigue crack propagation in heterogeneous geomaterials under varied loads using displacement discontinuity method. J. Rock Mesh. Geotech. Eng. 15 (3), 702–716.
Banadaki, M.D., 2011. Stress-wave induced fracture in rock due to explosive action. University of Toronto.
Bhagat, N.K., Mishra, A.K., Singh, R.K., Sawmliana, C., Singh, P.K., 2022. Application of logistic regression, CART and random forest techniques in prediction of blast-induced slope failure during reconstruction of railway rock-cut slopes. Eng. Fail. Anal. 137, 106230.
Bird, R., Paluszny, A., Thomas, R.N., Zimmerman, R.W., 2023. Modelling of fracture intensity increase due to interacting blast waves in three-dimensional granitic rocks. Int. J. Rock. Mech. Min. Sci. 162, 105279.
Chen, D., Wang, E.Y., Li, N., 2021. Rupture process assessment of rock bursts in a coal mine: Inversion of source parameters and the slip distribution on the rupture surface. Eng. Fail. Anal. 130, 105741.
Cordero, J.A.R., Sanchez, E.C.E., Roehl, D., 2019. Hydromechanical modeling of unrestricted crack propagation in fractured formations using intrinsic cohesive zone model. Eng. Fract. Mech. 221, 106655.
Feng, C., Li, S.H., Liu, X.Y., Zhang, Y.N., 2014. A semi-spring and semi-edge combined contact model in CDEM and its application to analysis of Jiweishan landslide. J. Rock Mesh. Geotech. Eng. 6 (1), 26–35.
Fukuda, D., Liu, H.Y., Zhang, Q.B., Zhao, J., Kodama, J.I., Fujii, Y., Chan, A.H.C., 2021. Modelling of dynamic rock fracture process using the finite-discrete element method with a novel and efficient contact activation scheme. Int. J. Rock. Mech. Min. Sci. 138, 104645.
Gharehdash, S., Barzegar, M., Palymskiy, I.B., Fomin, P.A., 2020. Blast induced fracture modelling using smoothed particle hydrodynamics. Int. J. Impact. Eng. 135, 103235.
Hajibagherpour, A.R., Mansouri, H., Bahaaddini, M., 2020. Numerical modeling of the fractured zones around a blasthole. Comput. Geotech. 123, 103535.
Han, H.Y., Fukuda, D., Liu, H.Y., Salmi, E.F., Sellers, E., Liu, T.J., Chan, A., 2020a. FDEM simulation of rock damage evolution induced by contour blasting in the bench of tunnel at deep depth. Tunn. Undergr. Space. Technol. 103, 103495.
Han, W., Jiang, Y.J., Luan, H.J., Du, Y.T., Zhu, Y.G., Liu, J.K., 2020b. Numerical investigation on the shear behavior of rock-like materials containing fissure-holes with FEM-CZM method. Comput. Geotech. 125, 103670.
Han, H.Y., Fukuda, D., Xie, J.B., Salmi, E.F., Sellers, E., Liu, H.Y., An, H.M., Chan, A., 2023. Rock dynamic fracture by destress blasting and application in controlling rockbursts in deep underground. Comput. Geotech. 155, 105228.
Jayasinghe, L.B., Shang, J.L., Zhao, Z.Y., Goh, A.T.C., 2019. Numerical investigation into the blasting-induced damage characteristics of rocks considering the role of in-situ stresses and discontinuity persistence. Comput. Geotech. 116, 103207.
Jiang, X.D., Xue, Y.G., Kong, F.M., Gong, H.M., Fu, Y.S., Zhang, W.M., 2023. Dynamic responses and damage mechanism of rock with discontinuity subjected to confining stresses and blasting loads. Int. J. Impact. Eng. 172, 104404.
Kuhlemeyer, R.L., Lysmer, J., 1973. Finite element method accuracy for wave propagation problems. J. Soil Mech. Found. Divis. 99 (5), 421–427.
Lak, M., Marji, M.F., Bafghi, A.Y., Abdollahipour, A., 2019a. Analytical and numerical modeling of rock blasting operations using a two-dimensional elasto-dynamic Green's function. Int. J. Rock. Mech. Min. Sci. 114, 208–217.
Lak, M., Marji, M.F., Bafghi, A.Y., Abdollahipour, A., 2019b. Discrete element modeling of explosion-induced fracture extension in jointed rock masses. J. Min. Environ. 10, 125–138.
Lin, Q.D., Feng, C., Zhu, X.G., Zhang, G.H., Li, S.H., 2022a. Evolution characteristics of crack and energy of low-grade highway under impact load. Int. J. Pavement Eng. 23 (9), 3182–3197.
Lin, Q.D., Li, S.H., Gan, Y.D., Feng, C., 2022b. A strain-rate cohesive fracture model of rocks based on Lennard-Jones potential. Eng. Fract. Mech. 259, 108126.
Liu, J., Wang, Z., Xiong, J., Yin, J.W., 2022. A near-field overpressure estimation equation of cylindrical charge explosive air blast. Trans. Beijing Inst. Technol. 42 (9), 918–927.
Liu, L., Zhang, P.R., Xie, P., Ji, S.Y., 2020. Coupling of dilated polyhedral DEM and SPH for the simulation of rock dumping process in waters. Powder. Technol. 374, 139–151.
Ma, T.H., Li, F.J., Yang, Y.H., Li, L.M., 2022. Study on energy evolution and crack propagation of rock mass under single hole uncoupled charge blasting. Appl. Eng. Sci. 11, 100112.
Mardalizad, A., Saksala, T., Manes, A., Giglio, M., 2020. Numerical modeling of the tool-rock penetration process using FEM coupled with SPH technique. J. Pet. Sci. Eng. 189, 107008.
Nairn, J.A., Aimene, Y.E., 2021. A re-evaluation of mixed-mode cohesive zone modeling based on strength concepts instead of traction laws. Eng. Fract. Mech. 248, 107704.
Ni, K.S., Yang, J., Ning, Y.J., Kang, G., 2020. A modified sub-block DDA fracturing modelling method for rock. Eng. Anal. Bound. Elem. 111, 154–166.
Peng, X.Y., Chen, G.Q., Fu, H.Y., Yu, P.C., Zhang, Y.B., Tang, Z.C., Zheng, L., Wang, W., 2021. Development of coupled DDA-SPH method for dynamic modelling of interaction problems between rock structure and soil. Int. J. Rock. Mech. Min. Sci. 146, 104890.
Qin, M.Q., Yang, D.S., Chen, W.Z., Yang, S.Q., 2021. Hydraulic fracturing model of a layered rock mass based on peridynamics. Eng. Fract. Mech. 258, 108088.
Rezanezhad, M., Lajevardi, S.A., Karimpouli, S., 2019. Effects of pore-crack relative location on crack propagation in porous media using XFEM method. Theor. Appl. Fract. Mech. 103, 102241.
Saadat, M., Taheri, A., 2019. A cohesive discrete element based approach to characterizing the shear behavior of cohesive soil and clay-infilled rock joints. Comput. Geotech. 114, 103109.

Wang, Y.h., Nguyen, N.H.T., 2022. The effects of rock-infill interfacial properties on the compressive damage behaviour of flawed rocks: Results from a DEM study. Theor. Appl. Fract. Mech. 117, 103166.

Wang, G.L., Sun, F., Wang, R.Q., Cao, T.C., 2021a. Simulation of cryogenic fracturing of rock-like materials using material point method. J. Nat. Gas. Sci. Eng. 96, 104300.

Wang, H.C., Wang, Z.L., Wang, J.G., Wang, S.M., Wang, H.R., Yin, Y.G., Li, F., 2021b. Effect of confining pressure on damage accumulation of rock under repeated blast loading. Int. J. Impact. Eng. 156, 103961.

Wang, S., Li, D.Y., Li, Z.H., Liu, J.Z., Gong, S., Li, G.Y., 2021c. A rate-dependent model and its user subroutine for cohesive element method to investigate propagation and branching behavior of dynamic brittle crack. Comput. Geotech. 136, 104233.

Wu, Z.J., Ma, L.L., Fan, L.F., 2018. Investigation of the characteristics of rock fracture process zone using coupled FEM/DEM method. Eng. Fract. Mech. 200, 355–374.

Zhang, Q.L., Zhi, Z.H., Feng, C., Cai, Y.C., Pang, G.H., Yue, J.C., 2020a. Investigation of concrete pavement cracking under multi-head impact loading via the continuum-discontinuum element method. Int. J. Impact. Eng. 135, 103410.

Zhang, Y.M., Gao, Z.R., Li, Y.Y., Zhuang, X.Y., 2020b. On the crack opening and energy dissipation in a continuum based disconnected crack model. Finite. Elem. Anal. Des. 170, 103333.

Zhou, Y., Feng, S.W., Li, J.W., 2021. Study on the failure mechanism of rock mass around a mined-out area above a highway tunnel – Similarity model test and numerical analysis. Tunn. Undergr. Space. Technol. 118, 104182.

Zhu, F., Zhao, J.D., 2021. Peridynamic modelling of blasting induced rock fractures. J. Mech. Phys. Solids. 153, 104469.